

## THE DYNAMICS OF LOW-MASS MOLECULAR CLOUDS IN EXTERNAL RADIATION FIELDS

RICHARD P. NELSON<sup>1,2</sup> AND WILLIAM D. LANGER<sup>3</sup>

MS 169-506, Jet Propulsion Laboratory, California Institute of Technology, Pasadena, CA 91109

Received 1996 June 19; accepted 1997 January 14

### ABSTRACT

We present the results of three-dimensional hydrodynamic calculations of the evolution of low-mass molecular clouds, performed using the numerical method of smoothed particle hydrodynamics. The clouds that we consider are subject to heating by the interstellar radiation field and by cosmic rays. They are able to cool through molecular line emission (primarily CO and its isotopes) and by emission from the fine structure lines of C<sup>+</sup> and O I. We also include gas-dust thermal coupling in our models. A simplified chemical network is incorporated that models the conversion between C<sup>+</sup> and CO, where the chemical balance is determined by the local flux of dissociating radiation. Calculations are performed for initially uniform density clouds, with masses in the range  $M = 100\text{--}400 M_{\odot}$ , sizes in the range  $R = 1.7\text{--}3.4$  pc, with the initial number density in all cases being  $n = 100 \text{ cm}^{-3}$ . We performed calculations for clouds with different geometrical shapes: spherical, prolate, and oblate. Additionally, we considered the effects of an anisotropic radiation field on the cloud evolution.

These are the main results:

1. Clouds that are initially Jeans stable are able to collapse because of the coupling between the dynamical and thermal evolution. This collapse results in core-halo structure where we have a cold, dense, CO core surrounded by a warmer, tenuous, C<sup>+</sup> envelope.
2. A pressure gradient is set up in the clouds by the attenuation of the UV radiation field. When a cloud is anisotropically heated, this pressure gradient leads to the formation of a highly flattened cloud core when it collapses.
3. The combined thermal and dynamical evolution of the prolate and oblate clouds leads to the formation of highly elongated or flattened structures. These structures are able to fragment, typically with four to eight subcondensations forming, which have masses in the range 3–7.5  $M_{\odot}$ .

*Subject headings:* hydrodynamics — ISM: clouds — ISM: globules — molecular processes — radiative transfer

### 1. INTRODUCTION

Much attention has been paid in recent years to the study of molecular cloud structure and star formation in intermediate-mass molecular cloud complexes such as Taurus and  $\rho$  Ophiuchi (Myers & Benson 1983; Loren 1989; Myers et al. 1991; Goodman et al. 1993). Observations of these regions indicate the existence of dense cores that appear to be the sites of ongoing star formation (Beichmann et al. 1986). The morphological complexity of these regions and the presence of young stellar objects, however, create problems when trying to understand the processes that lead to star formation, because of the difficulty in isolating localized regions of star formation. More recently, however, there have been a number of observational surveys of isolated, low-mass molecular clouds (e.g., Bok globules), which are aimed at examining the physical properties of such clouds (Clemens & Barvainis 1988; Clemens, Yun, & Heyer 1991; Bourke, Hyland, & Robinson 1995a; Bourke et al. 1995b). Whereas the dense cores in Taurus and Ophiuchus appear to be embedded within the overall cloud structure, and hence are shadowed from the interstellar radiation field, this is not the case with the isolated molecular clouds. Consequently, the fact that these

clouds are suffused with UV radiation may have an important impact on their dynamical, thermal, and chemical evolution. Typically, these isolated clouds are reported to have masses of  $M \sim 10 M_{\odot}$ , radii of  $R \sim 0.2\text{--}0.3$  pc, and are generally quite cold, with gas temperatures of  $T \sim 10$  K. These characteristics are derived from observations of CO line transitions. Far infrared observations of Bourke et al. (1995a) indicate that star formation is occurring in about half of their sample of 169 globules, with similar statistics being reported by Clemens & Barvainis (1988). In addition, CO observations suggest that these clouds have narrow line widths, indicative of quiescent gas in which the gas dynamical motions are approximately subsonic (Clemens & Barvainis 1988). The isolated nature of these clouds makes them ideal candidates for the detailed study of the star formation process.

A large number of calculations have been performed over the years, looking at the collapse and fragmentation of isothermal clouds. These calculations are relevant to the later stages of a molecular cloud's life, when the number density is  $n \approx 10^6 \text{ cm}^{-3}$  and the cloud has managed to divest itself of its dominant means of support against gravitational contraction (Boss 1986, 1993; Myhill & Kaula 1992; Bonnell et al. 1991; Nelson & Papaloizou 1993; Burkert & Bodenheimer 1993). These calculations are applicable to the study of the dense cores found within the intermediate-mass molecular clouds. One weakness of these models, however, is that they do not address the question of how the cloud came to

<sup>1</sup> r.p.nelson@qmw.ac.uk.

<sup>2</sup> Now at Astronomy Unit, School of Mathematical Sciences, Queen Mary and Westfield College, Mile End Road, London, E1 4NS.

<sup>3</sup> langer@langer.jpl.nasa.gov.

be in its assumed initial state. Attempts have been made to remedy this theory gap by modeling the evolution of molecular clouds from a much lower density phase (e.g., Gerola & Glassgold 1978; Prasad, Heere, & Tarafdar 1991). Although these calculations paid substantial attention to the details of the thermal and chemical evolution of the clouds, they were performed with one-dimensional hydrodynamics codes and so were unable to address the more interesting question of how the complex structure and fragmentation observed within molecular clouds occurs.

Thermal cooling has been suggested as a means of initiating cloud collapse (Glassgold & Langer 1976; Chieze & Pineau de Fôrets 1987; Tohline et al. 1987) and for inducing fragmentation of low-mass clouds (Chieze & Pineau de Fôrets 1987). It has been shown that in cooling regimes, where the effective adiabatic exponent is less than 1, an otherwise stable, wide range of cloud masses can be induced to collapse (Christodoulou & Tohline 1990). These studies, however, used simplified thermodynamics and/or analytical equilibrium models to explore the effects of cooling. The effects of cooling on the dynamical evolution of molecular clouds were examined by Monaghan & Lattanzio (1991), using a multidimensional hydrodynamics code with cooling by CO line emission. It was found that the clouds fragmented easily as a result of the cooling, but the important effects of heating by background UV radiation were neglected in this study. Calculations were also performed by Arcoragi et al. (1991), where they looked at the dynamical evolution of elongated clouds with different values of polytropic exponent,  $\gamma$ , in order to mimic heating and cooling of the gas. These calculations were designed to address the issue of how much fragmentation occurred as a function of  $\gamma$  and so are directed at answering different questions to those posed in this paper.

The potential role that the chemical structure and evolution plays in the dynamical fate of molecular clouds is that different chemical species have different cooling properties as a function of density and temperature. Several groups have developed time-dependent, but nondynamical, chemical models (Prasad & Huntress 1980; Graedel, Langer, & Frerking 1982; Millar et al. 1991), and Gerola & Glassgold (1978), Tarafdar et al. (1985), and Prasad et al. (1991) studied the chemical abundances of molecular clouds as they underwent gravitational collapse. Others have imposed a specific dynamical motion such as transport and turbulent mixing on the chemically evolving gas (Herbst & Leung 1986; Charnley et al. 1988; Xie et al. 1995). To date, however, no group has yet tackled the problem of how the dynamical, thermal, and chemical processes couple to drive the evolution of a molecular cloud, using multidimensional computer simulations.

The calculations presented in this paper represent our first step in performing hydrodynamic simulations of evolving molecular clouds that take into account the thermal and chemical evolution. Our guiding philosophy in this work is to take a step-by-step approach to increasing the complexity of our models at each stage, where the work presented here consists of the simplest cases that we have studied so far. The clouds that we consider are isolated, low-mass, molecular clouds, which are subject to heating by the interstellar radiation field. These were chosen because they represent a class of clouds in which the thermal pressure plays an important role in providing support against gravitational collapse (Clemens & Barvainis 1988). In more

massive clouds, the thermal pressure is negligible compared with the turbulent support. The physical processes that we include in our models are cooling due to molecular line emission and line emission from C<sup>+</sup> and O I, gas-dust thermal coupling, heating due to cosmic-ray ionization and due to the formation of molecular hydrogen on grains, and heating by the interstellar radiation field. A simplified chemical network is incorporated, which models the conversion of C<sup>+</sup> to CO, and vice versa, where the intermediate chemical pathways are parameterized rather than being explicitly included. We consider cloud masses in the range  $M = 100\text{--}400 M_{\odot}$  and sizes of  $L = 1.7\text{--}3.4$  pc. In each case, the density distribution is initially uniform, with  $n = 100 \text{ cm}^{-3}$ . Clouds of different geometrical shape are considered: spherical, prolate, and oblate, because observations indicate that many isolated clouds are elliptical, with typical axial ratios being  $a/b = 2$  (Clemens & Barvainis 1988). A more recent paper (Ryden 1996) reaches similar conclusions and, via a detailed analysis of cloud shapes, indicates that the clouds are more likely to be prolate, rather than oblate, objects viewed from different angles. In addition, we examine how changes in the external radiation flux, dust temperature, and boundary conditions affect the results of the calculations, as well as the effects of an anisotropic radiation field.

The paper is organized as follows. The basic equations of the problem are given in § 2.1, the thermal model is presented in § 2.2, and the chemical model is presented in § 2.3. The numerical methods used are described in § 3, and the initial and boundary conditions for the calculations are given in § 4. The results of the numerical calculations are presented and analyzed in § 5, and finally, in § 6, we provide a brief discussion and summary of the main results of this work.

## 2. SETTING UP THE PROBLEM

In the following sections we describe the various physical processes that we have included in our models of low-mass molecular clouds.

### 2.1. Basic Equations

The continuity, momentum, and energy equations for a compressible fluid can be written

$$\frac{d\rho}{dt} + \rho \nabla \cdot \mathbf{v} = 0, \quad (1)$$

$$\frac{d\mathbf{v}}{dt} = -\frac{1}{\rho} \nabla P - \nabla \Phi + \mathbf{S}_{\text{visc}}, \quad (2)$$

$$\frac{d\mathcal{U}}{dt} + \frac{P}{\rho} \nabla \cdot \mathbf{v} = \frac{\Gamma - \Lambda}{\rho}, \quad (3)$$

where

$$\frac{d}{dt} = \frac{\partial}{\partial t} + \mathbf{v} \cdot \nabla \quad (4)$$

denotes the convective derivative,  $\rho$  is the density,  $\mathbf{v}$  is the velocity,  $P$  is the pressure,  $\mathbf{S}_{\text{visc}}$  represents the viscous forces,  $\mathcal{U}$  is the internal energy per unit mass, and  $\Phi$  is the gravitational potential.  $\Gamma$  and  $\Lambda$  represent nonadiabatic heating and cooling processes, respectively. The chemical rate equation is written in the usual form:

$$\frac{dX_i}{dt} = nK_i, \quad (5)$$

where  $X_i$  is the fractional abundance of chemical species  $i$ ,  $K_i$  is the associated chemical reaction rate, and  $n$  is the total number density. This set of equations is supplemented by an equation of state, which for a perfect gas may be written

$$P = \frac{\mathcal{R}}{\mu} \rho T = K(S)\rho^\gamma, \quad (6)$$

where  $\mathcal{R}$  is the gas constant,  $\mu$  is the mean molecular weight,  $T$  is the temperature,  $K(S)$  is a function of the entropy, and  $\gamma$  is the ratio of the specific heats. For a perfect monatomic gas,  $\gamma = 5/3$  and is constant. For a gas composed of atoms or molecules with energy levels that may be excited, the specific heats are a function of temperature and pressure, and  $\gamma$  may fall below  $\gamma = 5/3$  when the temperature is such that the energy levels may be excited. The models considered in this paper are for low-temperature clouds, so that the kinetic temperature is below that necessary to excite the rotational and vibrational states of  $H_2$ . Thus, we take the value  $\gamma = 5/3$ .

## 2.2. The Thermal Model

The thermal model that has been incorporated in the work presented here is based on the calculations of Goldsmith & Langer (1978, hereafter GL78), along with some modifications and extensions that allow us to calculate the thermodynamics of initially diffuse molecular clouds more realistically. Those aspects of GL78 that we have included are molecular line cooling due a variety of molecular species, heating from cosmic-ray ionization and the formation of molecular hydrogen on grains, and gas-dust interactions that may either heat or cool the gas depending on the temperature difference between the gas and the dust. Additionally, we have included cooling due to radiation from the fine structure lines of  $C^+$  and  $O\,\text{I}$ , the two most important coolants in the low-density gas for  $T \lesssim 200$  K. The novel aspect of our work, however, is the inclusion of heating due to an external UV field. Each of these effects are described in greater detail below.

### 2.2.1. Molecular Line Cooling

Rather than calculate the total molecular line cooling as a sum of contributions from the individual molecular species, we have instead opted to use an analytical fit to the total cooling curve presented in GL78. This analytical fit is of the form

$$\Lambda_{\text{mol}} = \alpha \left( \frac{T_g}{10 \text{ K}} \right)^\beta \left( \frac{n}{\text{cm}^{-3}} \right)^\delta \text{ergs cm}^{-3} \text{s}^{-1}, \quad (7)$$

where we have defined  $\alpha = 5.0 \times 10^{-30} \text{ ergs cm}^{-3} \text{s}^{-1}$ ,  $\beta = 0.6 + 0.41 \log_{10}(n)$ , and  $\delta = 2.3 - 0.18 \log_{10}(n)$ , and  $n = n(H_2)$ . In this paper we consider clouds that are composed of molecular hydrogen, with a few trace species. Consequently, the equality  $n = n(H_2)$  holds throughout. Comparisons of equation (7) with cooling functions calculated using the method described in GL78 indicate that an excellent approximation to the molecular cooling is obtained by using this analytical fit. The comparison was performed over a range of  $n = 10-10^7 \text{ cm}^{-3}$  and a range of temperatures  $T = 10-100$  K. We also note that the density dependence of equation (7) has the correct limiting behavior in both the optically thin and the optically thick regimes, so that optical depth effects are included in this approximation to the cooling. Comparison with the results in GL78 show that  $^{12}\text{CO}$  and its isotopes do most of the cooling until very

high densities, at which point other molecules contribute. Here we calculate only the CO abundance explicitly, but at very high  $n$  these other molecules increase in abundance proportionately to CO.

### 2.2.2. Cooling Due to $C^+$ and $O\,\text{I}$

The cooling functions due to the collisional excitation of  $C^+$  and  $O\,\text{I}$  were taken from Chieze & Pineau des Fôrets (1987). We have modified the cooling function for  $C^+$ , however, to take into account the process of collisional de-excitation at higher densities that were not included in the original formula. The rate of cooling due to  $C^+$  is written as

$$\Lambda_{C^+} = [2.2 \times 10^{-23} n_H (1 - f/2) n(C^+) \exp(-92/T)] / \{1 + (n/n_{\text{crit}})[1 + 2 \exp(-92/T)]\}, \quad (8)$$

where  $n_H = n(\text{H I}) + 2n(\text{H}_2)$ ,  $f = 2n(\text{H}_2)/n_H$ , and  $n_{\text{crit}}$ , the critical number density is taken to be  $n_{\text{crit}} = 3 \times 10^3 \text{ cm}^{-3}$  (Genzel 1991). The cooling function due to atomic oxygen is expressed as

$$\Lambda_{O\,\text{I}} = 10^{-26} n_H (1 - f/2) n(O\,\text{I}) [24 \exp(-228/T) + 7 \exp(-326/T)] T^{1/2} \text{ ergs cm}^{-3} \text{s}^{-1}, \quad (9)$$

where  $n(O\,\text{I})$  is the number density of oxygen. We neglect radiative trapping in equations (8) and (9), because it is unimportant for the low-mass ( $M < 10^3 M_\odot$ ) clouds considered here.

### 2.2.3. Surface Cooling Term

Below a certain density ( $n \approx 10 \text{ cm}^{-3}$ ), no equilibrium temperature exists between the heat sources and the  $C^+$  and  $O\,\text{I}$  cooling, so that excessive heating of the outer layers of our clouds may occur if the density decreases too much in these regions. This effect arises because of our limited treatment of the cooling and chemistry, which has ignored cooling by molecular hydrogen and other trace elements at high temperatures. In order alleviate this problem, we have included an artificial surface cooling term, which may be written

$$\Lambda_{\text{surf}} = 7.31 \times 10^{-25} n \exp(-200/T) \times \exp(-2\tau_{\text{uv}}) \text{ ergs cm}^{-3} \text{s}^{-1}. \quad (10)$$

The addition of this surface term ensures that the temperature at the edge of the cloud does not increase much above 100 K when the density in these regions drops to  $\lesssim 10 \text{ cm}^{-3}$ . This term usually enters during the later stages of our calculations, when the central regions of the cloud have undergone significant evolution.

### 2.2.4. Cosmic-Ray Heating

The cosmic-ray heating term is

$$\Gamma_{\text{cr}} = \zeta_p(\text{H}_2) \Delta Q_{\text{cr}} n \text{ ergs cm}^{-3} \text{s}^{-1}, \quad (11)$$

where  $\zeta_p(\text{H}_2)$  is the primary cosmic-ray ionization rate of  $\text{H}_2$ , and  $\Delta Q_{\text{cr}}$  is the energy deposited as heat as a result of this ionization. Following GL78, we adopt values of  $\zeta_p(\text{H}_2) = 2.0 \times 10^{-17} \text{ s}^{-1}$  and  $\Delta Q_{\text{cr}} = 20 \text{ eV}$ , giving a total cosmic-ray heating rate of  $\Gamma_{\text{cr}} = 6.4 \times 10^{-28} n \text{ ergs cm}^{-3} \text{s}^{-1}$ .

### 2.2.5. $H_2$ Formation Heating

An additional source of heating in molecular clouds is  $H_2$  formation on grains. Some fraction of the 4.48 eV binding energy of the released  $H_2$  molecule goes into kinetic energy

and is thus transferred to the gas as heat. In a steady state, under conditions where only cosmic rays destroy H<sub>2</sub> molecules, and at high densities where most of the hydrogen is in molecular form, the H<sub>2</sub> formation heating can be considered as another term in the cosmic-ray heating term (see discussion in GL78). Accordingly, we can write the heating rate as

$$\Gamma_{\text{H}_2} = \left( \frac{\Gamma_{\text{cr}}}{3} \right) \left( \frac{Q_{\text{H}_2}}{4.48 \text{ eV}} \right) \text{ergs cm}^{-3} \text{ s}^{-1}, \quad (12)$$

where  $Q_{\text{H}_2}$  is the energy released as heat. We adopt a value of  $Q_{\text{H}_2} = 2.0 \text{ eV}$  in the work presented here.

### 2.2.6. Gas-Dust Interactions

When the kinetic temperature of the gas molecules differs from that of the dust grains, there is a thermal energy exchange through collisions. Assuming that when a molecule hits a dust grain it sticks to it and is later reemitted carrying an energy  $\sim 3/2 T_d$ , where  $T_d$  is the dust temperature, one can estimate the rate of energy exchange between the gas and dust. Following GL78, we have employed an energy exchange rate given by

$$\Lambda_{gd} = 2.4 \times 10^{-33} T_g^{1/2} (T_g - T_d) n^2 \text{ ergs cm}^{-3} \text{ s}^{-1}. \quad (13)$$

We note that gas-dust interactions play a major role in the thermal evolution of the gas only when the number density becomes rather high (i.e.,  $n \geq 10^5 \text{ cm}^{-3}$ ), but once these higher densities have been achieved, the gas-dust interactions dominate because of their quadratic dependence on  $n$ . As a consequence of this coupling, we typically adopt a fixed dust temperature of  $T_d = 10 \text{ K}$ , since the dust is known to be much cooler in the high-density regions where it is well shielded from the external heat sources. In the outer layers of clouds, where the incident radiation flux is high, it is expected that the dust temperature will be considerably higher than in the more shielded regions, but because of the lower densities the role of the dust in the thermal and dynamical evolution is negligible.

### 2.2.7. Grain Photoelectric Heating

In isolated molecular clouds, such as those considered here, the dominant contribution to the heating of the gas is through the photoejection of electrons from dust grains, caused by the incident UV photon component of the interstellar radiation field. We adopt the formula presented in Falgarone & Puget (1985), which follows from the work of de Jong (1977):

$$\Gamma_{pg} = 6.0 \times 10^{-26} G_0 n \exp(-\langle K \rangle \tau_v) \text{ ergs cm}^{-3} \text{ s}^{-1}, \quad (14)$$

where  $G_0$  determines by what factor the incident UV flux differs from the standard interstellar value (Habing 1968),  $\tau_v$  is the visual extinction, and  $\langle K \rangle$  prescribes the enhanced extinction experienced by UV photons due to scattering as they penetrate the cloud. In reality, the value of  $K$  is frequency dependent and falls within the range  $1.85 \leq K \leq 3.7$  (Falgarone & Puget 1985). We accordingly adopted an average value of  $\langle K \rangle = 2.5$ .

In order to calculate the photoelectric heating of the gas at an arbitrary point within the cloud, it is necessary to calculate the total ultraviolet extinction to that point,  $\tau_{uv}$ ,

where  $\tau_{uv} = \langle K \rangle \tau_v$ . The equation for  $\tau_{uv}$  is usually written

$$\tau_{uv}(r) = 1.25 \times 10^{-21} \int_r^R 2n(r') dr', \quad (15)$$

which is appropriate to integrating along the radial direction in a spherically symmetric distribution of matter, such as in the calculations of Falgarone & Puget (1985). In the calculations presented here, however, we are considering an arbitrary distribution of matter in three spatial dimensions and so need to adopt a slightly different approach. Ideally, when calculating the heating due to an external UV flux at an arbitrary point within a three-dimensional cloud of arbitrary geometry and density distribution, one would like to integrate along every ray path to each point on the cloud surface, summing over the contributions from each of the paths. Obviously, this approach is computationally intractable, and so explicit approximations must be made. The approach that we have adopted is to calculate the optical depth along each of the coordinate directions,  $x$ ,  $y$ , and  $z$ . Starting at an arbitrary point in three dimensional space,  $x'$ ,  $y'$ ,  $z'$ , we integrate outwards from that point in both the positive and negative coordinate directions and consequently calculate six separate optical depths, which we denote as  $\tau_x^+$ ,  $\tau_x^-$ ,  $\tau_y^+$ ,  $\tau_y^-$ ,  $\tau_z^+$ , and  $\tau_z^-$ . In this notation,  $\tau_x^+$  denotes the optical depth calculated along the positive  $x$ -direction from the arbitrary point  $x'$ ,  $y'$ ,  $z'$ , to the cloud surface at  $X_{\max}$ ,  $y'$ ,  $z'$ . Similarly,  $\tau_x^-$  denotes the optical depth along the negative  $x$ -direction to the cloud surface. The notation carries through for the other coordinate directions. Mathematically then,  $\tau_i^\pm$  may be expressed as

$$\tau_x^+(x', y', z') = 1.25 \times 10^{-21} \int_{x'}^{X_{\max}} 2n(x, y', z') dx, \quad (16)$$

and similar equations follow for each of the other  $\tau_i^\pm$ .

Having obtained these six estimates of the optical depth along the individual coordinate directions, we then calculate the UV heating rate as an average of the heating rates along each direction:

$$\begin{aligned} \Gamma_{pg} = 6.0 \times 10^{-26} G_0 n (\text{H}_2)^{\frac{1}{6}} & [\exp(-\tau_x^+) + \exp(-\tau_x^-) \\ & + \exp(-\tau_y^+) + \exp(-\tau_y^-) \\ & + \exp(-\tau_z^+) + \exp(-\tau_z^-)] \text{ ergs cm}^{-3} \text{ s}^{-1}. \end{aligned} \quad (17)$$

In the limit of the optical depth going to zero, our heating rate converges to the value obtained using equation (14) and represents an average of the contributions to the UV flux from each direction. By integrating along the Cartesian coordinate directions, we make a reasonable estimate of the path length to the nearest point on the cloud surface, from which we expect the largest contribution to the UV heating to originate, at least when the geometry of the cloud surface is of a simple form, as is the case with the spheroidal clouds considered in this work.

### 2.3. The Chemical Model

We assume that our cloud is composed of molecular hydrogen, with trace quantities of carbon and oxygen. We do not include a treatment of the hydrogen chemistry, as H I and H<sub>2</sub> play no role at low temperature, but we do include a simplified treatment of the conversion of singly ionized carbon C<sup>+</sup> to carbon monoxide CO. In this case, the degree of conversion is governed by the local UV flux, since this determines the balance between the formation and disso-

ciation of CO. Our simplified chemical model assumes the direct conversion of  $\text{C}^+$  to CO, or vice versa, without accounting explicitly for the intermediate reactions (cf. Langer 1976). In this model the chemistry is initiated by a radiative association reaction  $\text{C}^+ + \text{H}_2 \rightarrow \text{CH}_2^+ + \text{photon}$  with a reaction rate coefficient  $k_0$ . This molecular ion rapidly converts to CH and  $\text{CH}_2$  via ion-molecule reactions with  $\text{H}_2$  and dissociative recombination with electrons. The carbon radicals will either react with atomic oxygen to form CO with a reaction rate coefficient  $k_1$  or undergo photodissociation at an effective rate  $\Gamma_{\text{CH}_x}$ . Obviously, the efficiency for forming CO depends on the relative efficiency of the former process versus destruction. Carbon monoxide is destroyed by photodissociation to form neutral carbon, which is assumed to convert immediately into  $\text{C}^+$  as the range of radiation wavelengths that ionize carbon is larger than that which photodissociates CO. While our model does not treat the formation of neutral carbon through the dissociation of CO or recombination of  $\text{C}^+$ , it does capture the essentials for forming CO in clouds. The equation describing the rate of production/destruction of CO that we employ is written

$$\frac{dn(\text{CO})}{dt} = k_0 n(\text{C}^+) n\beta - \Gamma_{\text{CO}} n(\text{CO}), \quad (18)$$

where  $k_0 = 5 \times 10^{-16} \text{ cm}^3 \text{ s}^{-1}$ ,  $\Gamma_{\text{CO}}$  is defined by the relation

$$\Gamma_{\text{CO}} = G_0 10^{-10} \exp(-\tau_{\text{uv}}) \text{ s}^{-1} \text{ molecule}^{-1}, \quad (19)$$

and  $\beta$  is defined by the expression

$$\beta = \frac{k_1 X(\text{O I})}{k_1 X(\text{O I}) + G_0 [\Gamma_{\text{CH}_x}/n(\text{H}_2)]}. \quad (20)$$

The definition of  $\Gamma_{\text{CH}_x}$  introduced in equation (20) is given by

$$\Gamma_{\text{CH}_x} = 5 \times 10^{-10} \exp(-\tau_{\text{uv}}), \quad (21)$$

and  $k_1$  takes the value  $k_1 = 5 \times 10^{-10}$ . The fractional abundance of the total carbon is assumed to be  $X(\text{C}_{\text{total}}) = 10^{-4}$ , and the fractional abundance of the total oxygen is assumed to be  $X(\text{O}_{\text{total}}) = 2 \times 10^{-4}$ . For CO photodissociation we have chosen a characteristic extinction value and do not treat the line self-shielding of CO (cf. Bergin, Langer, & Goldsmith 1995). Our goal is to model the onset of CO formation with increasing extinction and not to model exact CO profiles at this stage. Once CO forms it is fairly robust and exists throughout the interior. We have also neglected the role of  $\text{H}_3^+$  and  $\text{He}^+$  because these are more critical for determining the production of other trace molecules in the interior.

### 3. NUMERICAL METHOD

The set of equations described in the preceding sections are solved using smoothed particle hydrodynamics (SPH) (Lucy 1977; Gingold & Monaghan 1977). SPH uses particles to represent a subset of the fluid elements that arise in the Lagrangian description of a fluid. The version of SPH used in the calculations presented here is a conservative formulation of the method that employs variable smoothing lengths (Nelson & Papaloizou 1994). For the sake of brevity, we do not provide a detailed description of the method, but highlight only those points salient to the work

presented in this paper. A detailed description of the code is presented in Nelson & Papaloizou (1994), along with a number of test calculations.

In order for the method to be conservative, the smoothing lengths must be functions only of the interparticle separations. Accordingly, we find the  $N_{\text{TOL}}$  nearest neighbors and calculate the smoothing lengths,  $h_i$ , using the expression

$$h_i = \frac{1}{N_{\text{far}}} \sum_{n=1}^{N_{\text{far}}} \frac{1}{2} |\mathbf{r}_i - \mathbf{r}_n|, \quad (22)$$

where the summation is over the  $N_{\text{far}}$  most distant nearest neighbors of particle  $i$ . For the calculations presented here, we take  $N_{\text{TOL}} = 45$  and  $N_{\text{far}} = 6$ .

The numerical method employs an artificial viscosity term that allows shocks to be properly modeled. The magnitude of this viscosity is controlled by two parameters,  $\alpha$  and  $\beta$  (Nelson & Papaloizou 1994). We set the parameters to have the values  $\alpha = 0.5$  and  $\beta = 1.0$ .

The gravitational forces are calculated using an implementation of the Barnes-Hut hierarchical tree algorithm (Barnes & Hut 1986; Hernquist 1987). The interparticle potential was softened by the method of spline softening (Gingold & Monaghan 1977), with a constant value of the softening length used in each calculation. The value of the softening length is given by  $h_{\text{grav}} = 0.005R_{\text{cloud}}$ , where  $R_{\text{cloud}}$  is the initial radius of the cloud.

The number of particles used in each of the calculations were  $N = 28,421$  for the spherical clouds,  $N = 23,952$  for the prolate clouds, and  $N = 29,477$  for the oblate clouds.

#### 3.1. Grain Photoelectric Heating

In order to calculate the rate of heat deposition at the particle positions, it is first necessary to calculate the optical depth through the cloud and thus to calculate numerically an approximation to equations such as equation (16). We discretize the cloud by using a regular cubic grid that fits around the cloud boundary. The density in each cell is then calculated by taking the mean density of the particles contained within that cell. Cells that do not contain particles have their density calculated by taking the average density of the six adjacent cells in the  $x$ -,  $y$ -, and  $z$ -coordinate directions. The optical depth, along a given coordinate direction from the cloud surface to a given particle position within the cloud, is then approximated by summing over cells along that coordinate direction from the particle position to the cloud surface. The total UV extinction along the positive  $x$ -direction for a particle located at  $\mathbf{r}_i$  is then given by the expression

$$\tau_x^+(\mathbf{r}_i) = 1.25 \times 10^{-21} \sum_{k=1}^{N_{\text{grid}}} 2n_k \Delta x, \quad (23)$$

where  $N_{\text{grid}}$  is the number of cells from the particle position  $\mathbf{r}_i$  to the cloud boundary, traveling in the positive  $x$ -direction,  $n_k$  is the number density of cell  $k$ , and  $\Delta x$  is the grid size. Thus, expression (23) represents a discretization of equation (16). Similar expressions follow for the optical depths in the other coordinate directions.

An alternative method of calculating the optical depths along the various lines of sight would be to interpolate the density of the SPH particles onto the chosen ray paths extending from the cloud surface to the particle positions. This method would probably be a little more accurate but

would also be considerably more time consuming computationally. Because we are attempting to obtain a general picture of cloud evolution with the calculations presented here, and not a highly accurate series of models, we use the quicker method of calculating the optical depths described above, which still produces reasonable estimates of the ultraviolet extinction.

### 3.2. Time Integration

The standard second-order leapfrog scheme, with the modification proposed by Hernquist & Katz (1989) for estimating time-centered velocities in the viscous pressure term was used to integrate the momentum and particle-shift equations. The time step size was determined by the expression given in Nelson & Papaloizou (1993).

With the inclusion of heating and cooling terms, it is necessary to integrate the energy equation implicitly, due to the disparity in the dynamical and thermal timescales (Monaghan & Varnas 1988; Hernquist & Katz 1989; Monaghan & Lattanzio 1991). We write the energy equation in the form

$$f(T_i^{n+1}) = u_i(T_i^{n+1}) - u_i(T_i^n) - \delta t Q_i^n + \delta t \left[ \frac{\Lambda(T_i^n, n_i^n) - \Gamma(n_i^n)}{\rho_i^n} \right], \quad (24)$$

where  $Q_i^n$  is the  $PdV$  work plus viscous dissipation, and the superscripts  $n$  and  $n+1$  refer to the  $n$ th and the  $(n+1)$ th time steps. Equation (24) is a nonlinear equation in  $T_i$  and so must be solved iteratively. We have employed a simple bisection scheme for this purpose in the calculations presented here, though we have subsequently implemented a combination of the bisection and the false position method for future work. The use of a simple iterative scheme reflects the exploratory nature of the calculations presented in this paper. We use the method of Monaghan & Lattanzio (1991) to bracket the root of this equation, and then iterate until the condition

$$\left| \frac{f(T_i^{n+1})}{u_i(T_i^n) + \delta t Q_i^n} \right| < 0.001 \quad (25)$$

has been satisfied. Typically, about six iterations were required to achieve convergence.

We also integrate the chemical evolution equation implicitly. The chemical evolution equation is written in the form

$$f[n(\text{CO})^{n+1}] = n(\text{CO})^{n+1} - n(\text{CO})^n - \delta t [k_0 n(\text{C}^+)^{n+1} n^\beta - \Gamma_{\text{CO}}^n n(\text{CO})^{n+1}], \quad (26)$$

where the definition of the various symbols is the same as that given in § 2.3, and the  $n$  and  $n+1$  superscripts have the same meaning as above. The iterative scheme employed is similar to that used for the thermal energy equation. The criterion for convergence is

$$\left| \frac{f[n(\text{CO})_i^{n+1}]}{n(\text{CO})^n + \delta t [k_0 n(\text{C}^+)^{n+1} n^\beta - \Gamma_{\text{CO}}^n n(\text{CO})^{n+1}]} \right| < 0.001. \quad (27)$$

### 4. INITIAL AND BOUNDARY CONDITIONS

The clouds considered in this paper fall into three main geometrical categories: spheres, prolate spheroids, and

oblate spheroids. The prolate and oblate spheroids each had initial axial ratios  $a/b = 2$ . The particles for each of these three geometrical forms were initially set up by placing them on a body-centered cubic lattice, subject to the condition that they lie within the volume described by a boundary of the required spherical or spheroidal geometry.

The initial velocity of all particles was set to zero, and the clouds' masses and radii were chosen to ensure that the initial number density  $n = 100 \text{ cm}^{-3}$  for all cases considered. The initial temperature of each cloud was set to be  $T = 60 \text{ K}$ , though the thermal timescale is sufficiently short that the clouds develop a thermal structure that is close to that of thermal equilibrium within one time step. At this point, central temperatures are approximately 50 K, and temperatures at the surface are about 70 K. The thermal profile arises because of the attenuation of radiation as it penetrates the cloud. When we discuss the results of the calculations in later sections, reference is made to the initial thermal state of the cloud. When making these remarks, we are referring to the thermal state after a single time step.

The initial chemical structure of the clouds assumes that hydrogen is in molecular form and that the carbon is in its singly ionized ( $\text{C}^+$ ) state throughout the cloud. In all cases considered, the ultraviolet extinction and density are initially low enough such that CO is unable to form efficiently until the clouds have undergone sufficient dynamical evolution to evolve out of the diffuse stage, typically a couple of million years for the masses and densities considered here.

The boundary condition employed is a constant volume boundary condition. This was imposed by reflecting any particles that strayed outside of a predetermined volume of a given geometry (i.e., spherical, prolate, or oblate), back into the computational domain. The particles were not reflected back elastically, but were instead reflected back with only 10% of their original velocity, since previous tests of this boundary condition indicate that spurious sound waves may be generated otherwise (Nelson 1994). Test calculations were performed to see if changing the boundary condition altered the nature of the results obtained. A free boundary was used in these cases. As one might expect, the external cloud layers tended to evaporate outwards when a free boundary was used. The central regions of the clouds, however, appeared to be largely unaffected in their dynamical evolution. A more detailed description of one such test calculation is given in § 5.3.4.

### 5. NUMERICAL CALCULATIONS

In the following subsections, we describe the results of the numerical calculations. The calculations are subdivided into four distinct classes: spherical clouds with isotropic radiation fields, spherical clouds with anisotropic radiation fields, prolate clouds, and oblate clouds. Representative runs from each of these classes are described and discussed in detail, and general trends which arise when the run parameters are changed are highlighted.

The heating and cooling rates per molecule of the different thermal processes are presented in Figure 1 as a function of  $T$  and  $n$ . Values of  $X(\text{C}^+) = X(\text{CO}) = 5 \times 10^{-5}$  were assumed in calculating the cooling rates. Each panel corresponds to a different gas temperature, which is shown at the top right of each panel, but  $T_d = 10 \text{ K}$  throughout. This figure is used to illustrate certain points that arise in the following sections when discussing the thermal evolution of the gas.

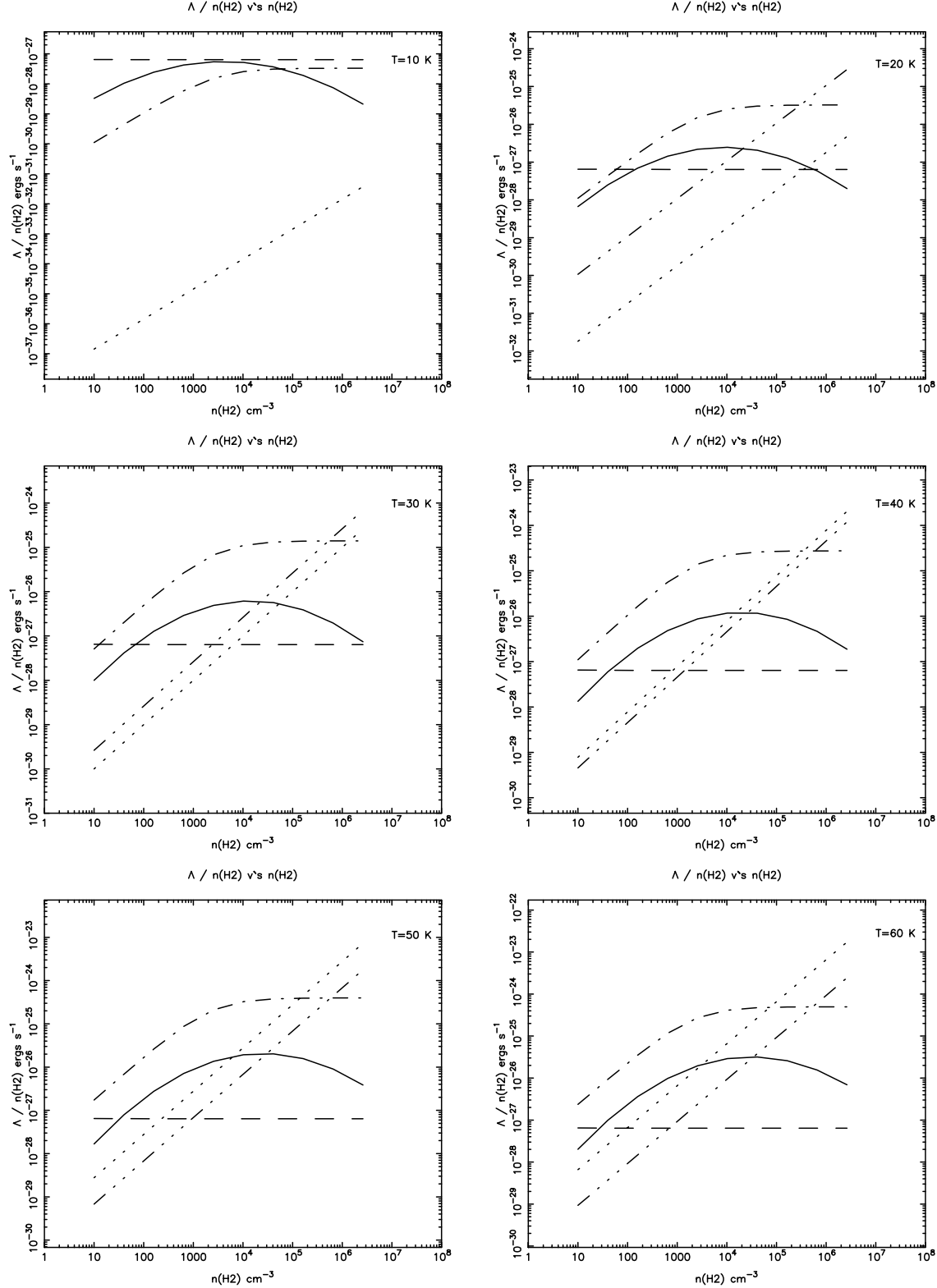


FIG. 1.—This figure shows the different contributions to the heating and cooling as a function of density and temperature. The  $\text{C}^+$  cooling is represented by the solid line, and the total molecular cooling by the dash-dotted line. The combined cosmic-ray and  $\text{H}_2$  formation heating is represented by the long-dashed line, and the oxygen cooling by the short-dashed line. The gas-dust cooling is represented by the dash-double-dotted line.

### 5.1. Spherical Clouds with Isotropic Radiation Fields

We performed a single calculation to study the dynamical evolution of a spherical cloud subject to heating by an isotropic, external radiation field. The motivation for per-

forming this calculation was twofold. First, we wished to examine the effect of including the heating and cooling mechanisms on the gravitational stability of a molecular cloud. In particular, we were interested in how the evolution

of this cloud would differ from that of an isothermal cloud that was otherwise identical. The comparison isothermal cloud has a temperature equal to the minimum temperature initially present within the heated and cooled cloud. Second, we wished to have a "standard" calculation that could be used to examine the thermal and chemical evolution of the cloud, without any additional complications. This calculation could then be used as a fiducial case, against which we could compare the different cloud models.

The "standard" cloud model has a mass of  $100 M_{\odot}$ , a radius of 1.69 pc, and an initial temperature of 60 K. We note, however, that after a single time step, a temperature profile is established within the cloud such that the maximum temperature at the outer edge is  $T_{\max} \approx 67$  K and the minimum temperature at the cloud center is  $T_{\min} \approx 54$  K. The value adopted for  $G_0$ , the parameter that determines the radiation field flux, is  $G_0 = 1$ , so that the radiation field is equal to the standard interstellar value. The cloud is taken to be initially composed of H<sub>2</sub>, with trace quantities of C<sup>+</sup> and O I present with the fractional abundances  $X(C^+) = 1 \times 10^{-4}$ , and  $X(O I) = 2 \times 10^{-4}$ , respectively. The density distribution is initially uniform, and the adoption of the above values for the mass and radius give a number density of  $n = 100 \text{ cm}^{-3}$ . The dust temperature is taken to be fixed at  $T_d = 10$  K.

The Jeans mass of a cloud with density  $\rho$  and sound speed  $c_s$  is given by the equation (Binney & Tremaine 1987)

$$M_J = \frac{1}{6} \pi \rho \left( \frac{\pi c_s^2}{G \rho} \right)^{3/2}. \quad (28)$$

For a cloud of  $n = 100 \text{ cm}^{-3}$  and temperature equal to  $T = 54$  K (which is equal to  $T_{\min}$  given above),  $M_J = 488 M_{\odot}$ . Also, the initial value of  $\alpha$ , which is the ratio of the thermal to the absolute value of the gravitational energy, is  $\alpha = 2.36$  after the initial thermal profile has been established in the heated and cooled cloud. Consequently, if the cloud were to remain in its initial thermal state, it would not be expected to undergo gravitational collapse.

The results from this calculation are shown in Figures 2, 3, and 4, where the time evolution of the density, temperature, and chemical profiles through the cloud are displayed, respectively. Figure 5 shows the evolution of the central temperature as a function of the central number density. The top left panel of Figure 2 shows that the cloud is of uniform density initially. We see from the top left panel of Figure 4 that the carbon present within the cloud is in the form of C<sup>+</sup> during the early stages of the calculation, since the optical depth through the cloud is low enough initially that substantial dynamical evolution must occur before CO is able to form. It is apparent from the top left panel of Figure 3 that an initial temperature, and therefore thermal pressure, gradient is present within the cloud, with the outer edges of the cloud being warmer than the interior. This results from the attenuation of the radiation field as one goes deeper into the cloud from the surface.

As the cloud evolves forward in time, the density begins to rise in the central regions, both because of the cloud relaxing in its own gravitational potential well (because it is of uniform density initially) and because of the inward-pushing pressure gradient, as illustrated by the top right panel of Figure 2. As the central regions of the cloud continue to become more dense, the attenuation of the radiation field is gradually increased, and the cooling rate, due

exclusively to C<sup>+</sup> at this stage, is increased because of its strong density dependence. Consequently, the temperature decreases as a function of time and radius in the more centrally located regions of the cloud, reinforcing the action of the inward-pushing pressure wave, and gradually increasing the local dynamical influence of the gravitational forces. This decrease in temperature may be observed moving from the top left panel to the middle right panel in Figure 3. The top right panel of Figures 2 and 3 also show that the density in the outer regions of the cloud decreases, contemporaneously with the central density increasing, and that the temperature rises because of the increased ability of the UV field to penetrate the outer layers of the cloud, and the reduced C<sup>+</sup> cooling efficiency at lower densities.

The top right panel of Figure 4 shows that during this early time, when the central density has increased almost fourfold to  $n \approx 400 \text{ cm}^{-3}$ , the carbon still remains primarily in the form of C<sup>+</sup>. The chemical conversion becomes rapid when the central density reaches  $n \approx 800 \text{ cm}^{-3}$ , at about  $t = 2.65$  Myr. The carbon starts to undergo efficient chemical conversion in these regions, with the C<sup>+</sup> combining with H<sub>2</sub> to form hydrides that subsequently interact with O I to form CO molecules (see § 2.3). At this point in time the extinction is large enough that internal shielding of the UV field prevents the dissociation of CO molecules. Furthermore the density is now high enough that the chemical formation time is approximately a few  $\times 10^5$  yr or less, comparable to the dynamical time. (The conversion rate is controlled in part by the choice of the chemical rate constant,  $k_0$ , in eq. [18].) The middle panels of Figure 4 show the completion of the conversion, and the corresponding panels in Figure 2 show that this chemical change arises largely when the central density is greater than  $2 \times 10^3 \text{ cm}^{-3}$ .

Comparison of the density and chemical profiles show that the cloud evolves into a core/halo structure, consisting of a cold, dense core in which the carbon is in the form of CO molecules, surrounded by a warm, tenuous halo in which the carbon is in the form of C<sup>+</sup> (see the bottom left panels of Figs. 2, 3, and 4). We note that the attainment of central temperature values of  $T \approx 10$  K in the bottom left panel of Figure 3 arises as a result of thermal balance between cosmic-ray and H<sub>2</sub> formation heating, and CO cooling, for densities of  $n \approx 10^4 \text{ cm}^{-3}$  and temperatures of  $T \approx 10$  K. This balance may be observed in the top left panel of Figure 1. At these densities, the gas does not experience strong thermal coupling to the dust, so that gas-dust coupling does not contribute greatly to the thermal evolution at this stage. We also note that the UV field is no longer able to penetrate into these central regions, and so contributes little to the thermodynamic evolution of the inner parts of the cloud from now on. With core densities of  $n \approx 10^4 \text{ cm}^{-3}$ , and temperatures of  $T \approx 10$  K, gravitational forces now dominate the inner regions of the cloud. Consequently, material at the center of the cloud undergoes a period of very rapid contraction, with the density increasing by 6 orders of magnitude during the passing of only  $3 \times 10^5$  yr, as shown in the bottom panels of Figure 2. During this stage of rapid collapse, there is a slight increase in the temperature of gas in the central regions whose density is between  $10^4$  and  $10^5 \text{ cm}^{-3}$ . The temperature rises to between 10 and 20 K, and this effect is demonstrated in Figure 5. Detailed analysis of the heating and cooling rates indicates that the cosmic-ray heating and the molecular line

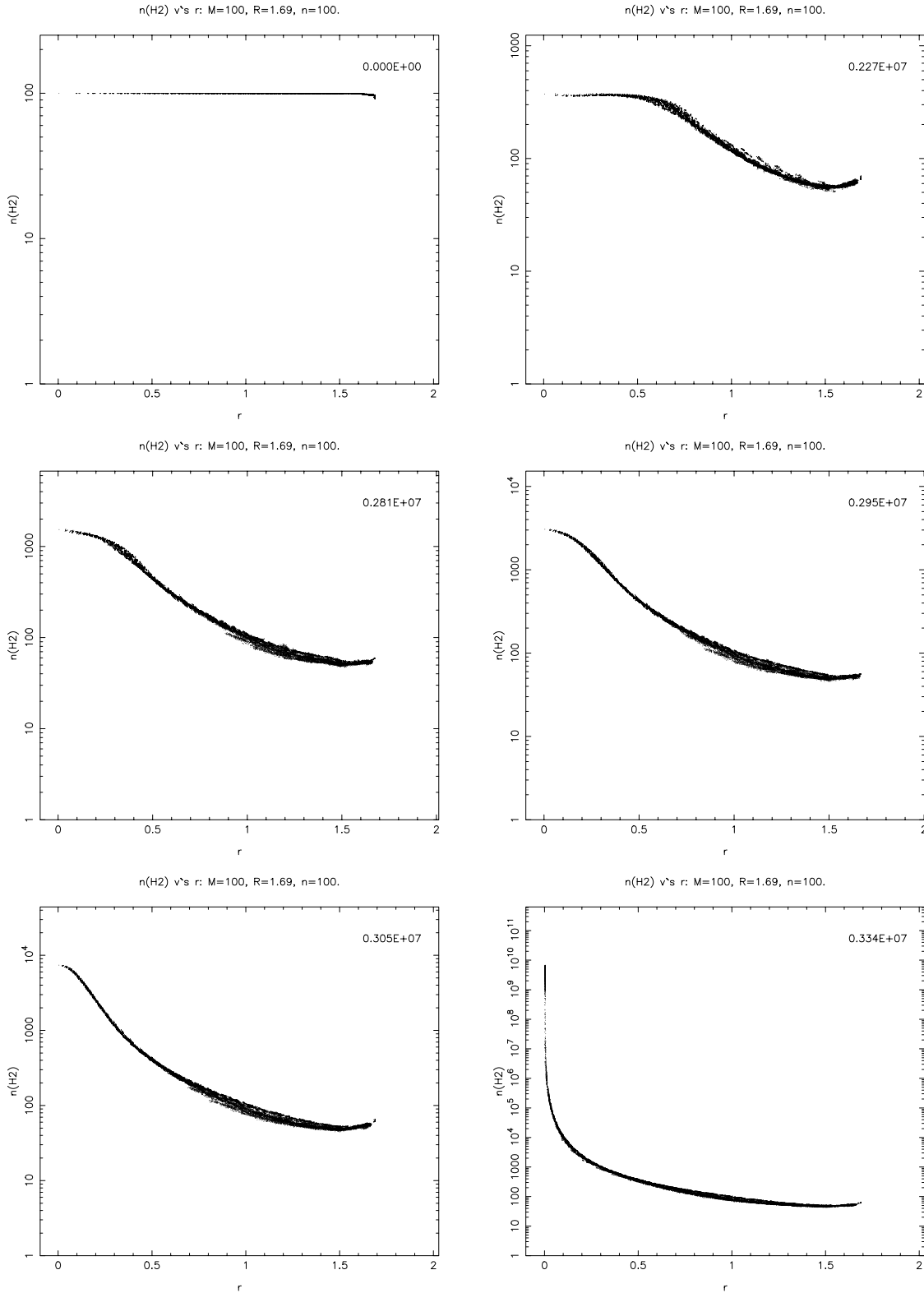


FIG. 2.—This figure shows the evolution of density  $n$  as a function of radius for the  $M = 100 M_{\odot}$  isotropically heated cloud. Times in years are shown at the top right corner of each panel.

cooling rates are in approximate balance in this region, as described above, with the other microphysical thermal effects playing almost no role. Consequently, the compressional heating of the gas is able to raise the temperature during the gravitational collapse of the core in those regions

where  $n$  is between  $10^4$  and  $10^5 \text{ cm}^{-3}$ . We remark that the viscous dissipation of energy due to the artificial viscosity is found to be a minor contributor to the heating during this stage, being typically *at least* a factor of 3 lower than the  $P dV$  work term. The material in the core with densities

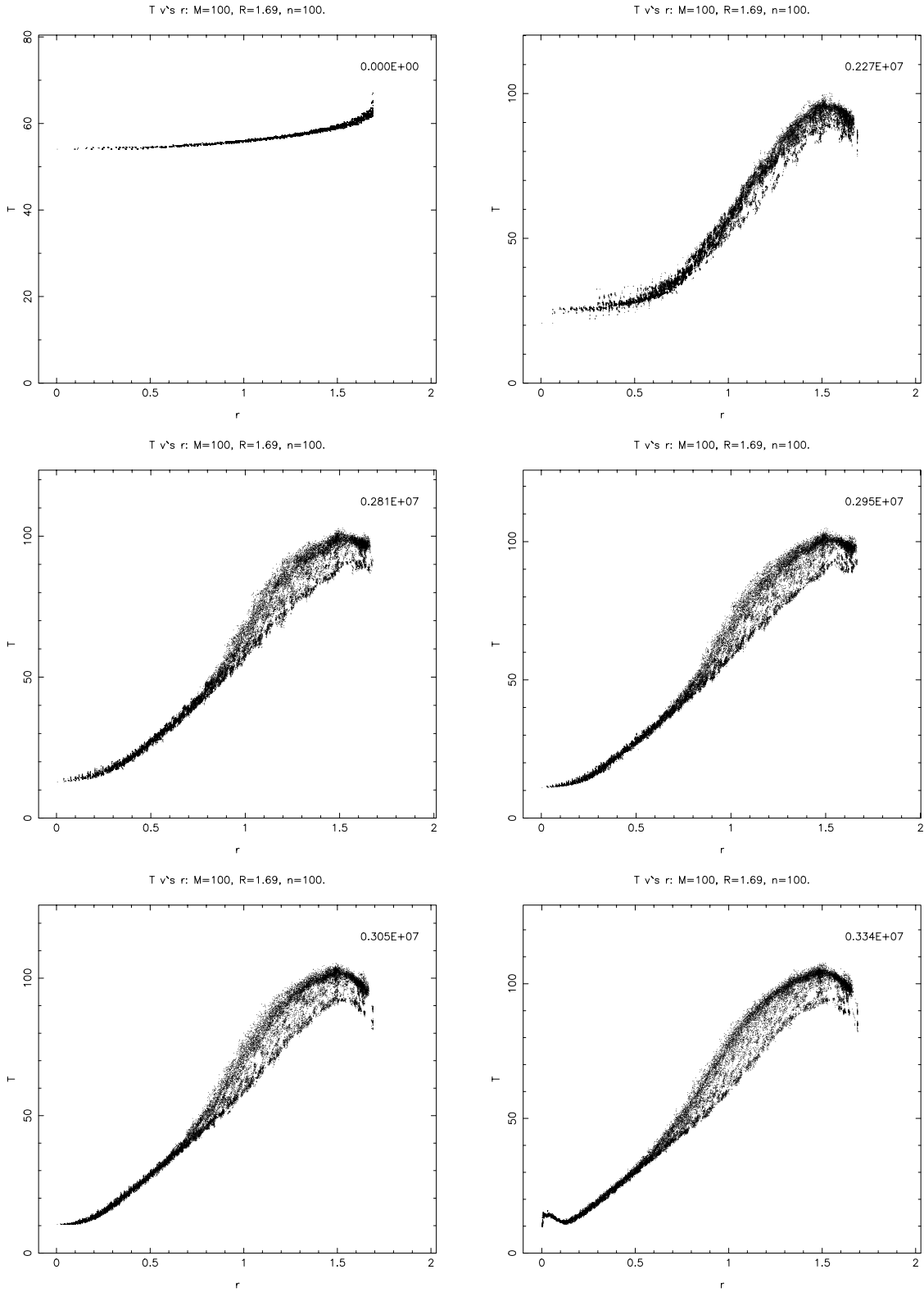


FIG. 3.—This figure shows the evolution of  $T$  as a function of radius for the  $M = 100 M_{\odot}$  isotropically heated cloud. Times in years are shown at the top right corner of each panel.

$n \gtrsim 10^6 \text{ cm}^{-3}$ , maintains a temperature of  $T = 10 \text{ K}$  because of the very strong coupling between the gas and dust at these higher densities.

The calculation was stopped when the central density reached  $n = 10^{10} \text{ cm}^{-3}$  because the time step size became prohibitively small. It is expected that the central regions

will continue to collapse, eventually forming a “protostar.” The eventual fate of the envelope cannot be definitively determined with this set of calculations for two reasons, one numerical, one physical. First, with such a small time step size, too many iterations would be required to determine the dynamical fate of the envelope. This problem could be

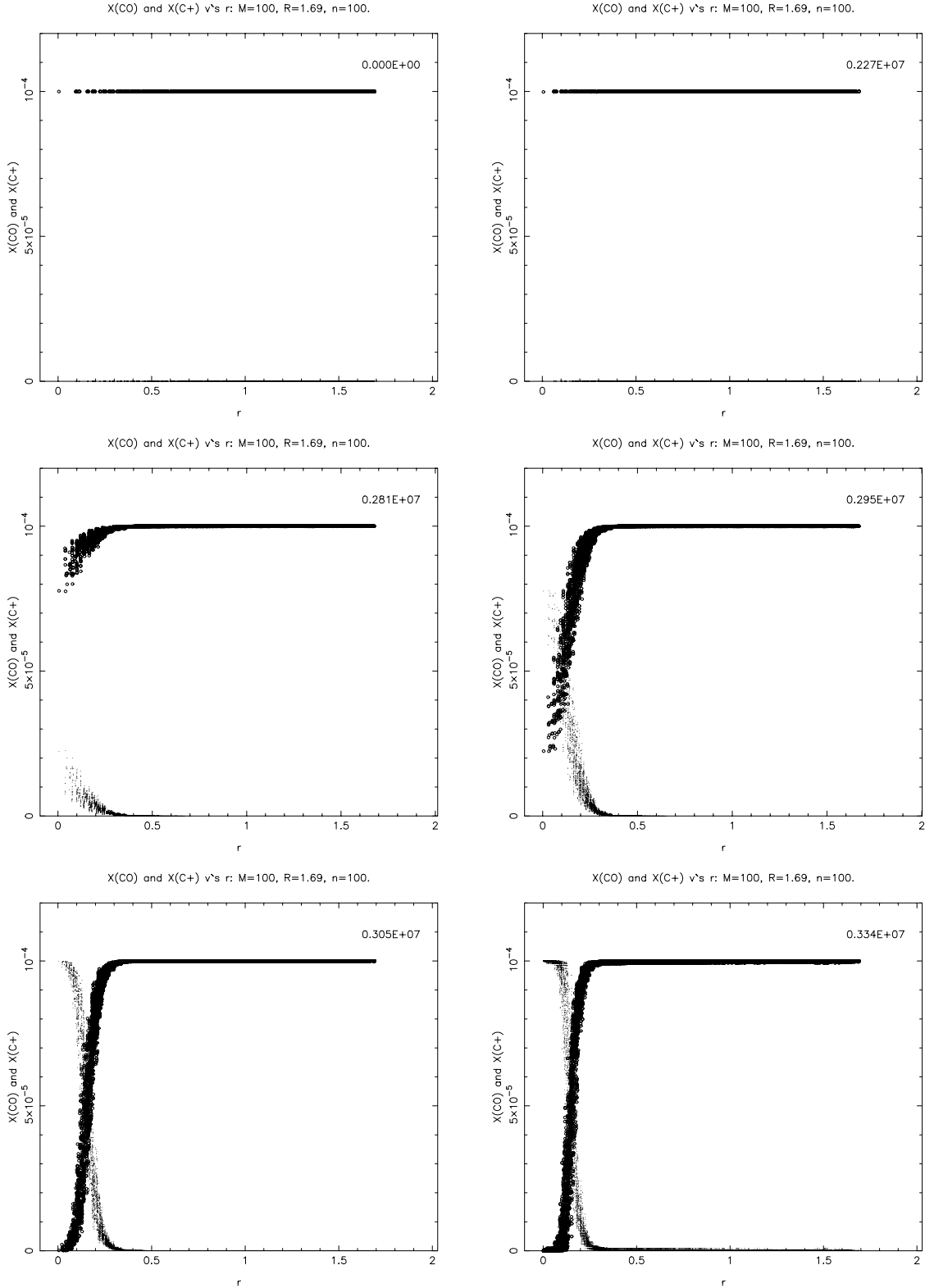


FIG. 4.—This figure shows the evolution of  $X(C^+)$  and  $X(CO)$  as a function of radius for the  $M = 100 M_\odot$  isotropically heated cloud. Times in years are shown at the top right corner of each panel.

alleviated, however, by replacing the dense core with a point mass accretion particle, similar to that used by Bate, Bonnell, & Price (1995). Second, we have only treated the thermochemical evolution of the lower density and higher temperature material near the surface in a very approximate fashion, so that a more detailed treatment of the micro-

physics would be required before statements about the long-term structure of the envelope could be made. It seems reasonable, however, to assume that a substantial part of the envelope will remain hydrostatically supported against collapse onto the central core through the attainment of higher temperatures.

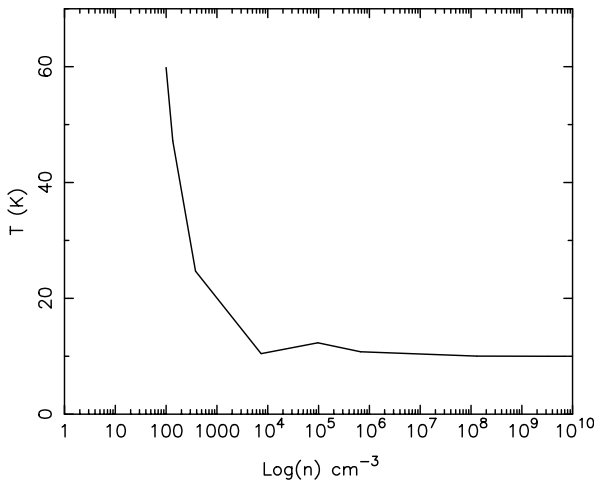


FIG. 5.—This figure shows the evolution of the central temperature as a function of the central number density for the  $M = 100 M_{\odot}$  spherical cloud.

We performed two additional calculations similar to that just described. This time, however, we did not include a full treatment of the microphysics, but instead assumed a simple equation of state. In one case, the gas was assumed to be isothermal, having a temperature of  $T = 54$  K throughout. This temperature is the minimum attained in the original cloud when close to thermal equilibrium. Our prediction of gravitational stability stated at the beginning of this section, based on the Jeans mass argument, was confirmed, since this cloud did *not* undergo gravitational collapse, but instead underwent a number of oscillations. We repeated this calculation with the modification that the temperature profile within the cloud at the start of the calculation was the same as that of the original cloud when close to thermal equilibrium, having a maximum temperature of  $T_{\max} = 67$  K at the outside edge and a minimum temperature of  $T_{\min} = 54$  K at the cloud center. The gas, however, was treated as being locally isothermal in that each fluid element maintained its original temperature throughout the calculation. This calculation was performed to see if including the initial temperature and pressure gradient present in the original calculation affected the gravitational stability of the isothermal cloud. It was found that the cloud was still stable against gravitational collapse, though the central densities attained during the oscillation of the cloud were slightly higher in this case than in the previous isothermal calculation. Thus, the existence of a temperature gradient has a noticeable but not crucial impact on this calculation, and is unable to induce gravitational instability without the gas being able to cool.

### 5.2. Spherical Clouds with Anisotropic Radiation Fields

Calculations were performed to study the dynamical evolution of spherical molecular clouds under the influence of anisotropic radiation fields. Having recognized the potential role of the pressure gradient created within a cloud when externally heated, in influencing the collapse of a cloud, we find it of interest to examine how anisotropy in the radiation field affects the form of the collapse. It is expected that many clouds will be subjected to spatial variations in their incident radiation fields due to being out of the Galactic plane, or due to O-B stars not being distributed

isotropically around the locations of many molecular clouds. For example, the molecular cloud L134N is known to be out of the Galactic plane and has an anisotropic radiation field (Laureijs et al. 1995).

The radiation field anisotropy was created by including the factor

$$(1 + \delta |\cos \theta|)$$

on the right-hand side of equation (14), where  $\cos \theta = z/r$  and  $\delta$  is a constant that determines the magnitude of the anisotropy. The inclusion of this factor in equation (14) is not intended to mimic the exact form of the anisotropic radiation fields that molecular clouds might be subject to, but rather to model their general effect.

Calculations were performed on clouds with masses  $M = 100, 200$ , and  $400 M_{\odot}$ . The initial number density of molecular hydrogen was  $n = 100 \text{ cm}^{-3}$  in each case, so that the cloud radii then took the values of  $R = 1.69, 2.13$ , and  $2.68 \text{ pc}$ , respectively. The dust temperature was fixed at  $T_d = 10 \text{ K}$ , and  $G_0 = 1$ . In the case of the  $M = 100$  and  $200 M_{\odot}$  clouds, we considered a value of the anisotropy parameter  $\delta = 0.5$ , so that the heating from above and below the cloud, along the  $z$ -direction, was increased by 50%. In the case of the  $M = 400 M_{\odot}$  cloud, values of  $\delta = 0.2$  and  $0.5$  were considered.

We discuss the  $M = 400 M_{\odot}, R = 2.68 \text{ pc}, \delta = 0.5$  case in some detail below, since this was the more interesting of the calculations performed. We make comparisons with other calculations, however, and attempt to draw conclusions about the trends observed when changing either the mass and radius, or the level of anisotropy in the radiation field.

In Figure 6 we present grayscale images of the molecular hydrogen number density,  $n$ , in the  $z = 0$  and  $y = 0$  planes of the cloud, at three different times during the calculation. The panels in the left-hand column are images representing  $n$  of material sampled in the vicinity of the  $z = 0$  plane, and the panels in the right-hand column sample  $n$  in the vicinity of the  $y = 0$  plane. Although this figure is unable to show the details of the calculation, it nonetheless illustrates the fact that the cloud collapses and forms an oblate core at its center. It should be noted that the levels represented by the grayscale change from panel to panel.

A more detailed view of the evolution of the cloud's density field is provided by Figure 7, where we have "zoomed in" on the central regions. This figure is similar to Figure 6, except that the panels correspond to different times during the calculation. It is immediately obvious from the top panels of Figure 7 that after  $t \approx 3 \text{ Myr}$ , a dense, toroidal structure surrounded by more tenuous material has formed near to the cloud center. At this point, the peak number density is  $n \approx 3 \times 10^3 \text{ cm}^{-3}$ . As time progresses, this dense toroidal structure continues to propagate in toward the cloud center, steepening in density as it does so. By the end of the calculation, after  $t \sim 3.4 \text{ Myr}$ , the dense ring has almost reached the center and has a number density of  $n \approx 3 \times 10^7 \text{ cm}^{-3}$ .

Figures 8 and 9 display plots of the temperature profile in the cloud at different times. In Figure 8, only particles that lie within a cylindrical distance of  $r = 0.2 \text{ pc}$  from the  $x$ -axis are plotted, against their  $x$ -coordinate value. Thus, because of the initial azimuthal symmetry of the cloud, this figure illustrates how the temperature profile of the cloud changes in the equatorial ( $z = 0$ ) plane as a function of time. Figure 9 is similar to Figure 8, except that it plots temperature versus

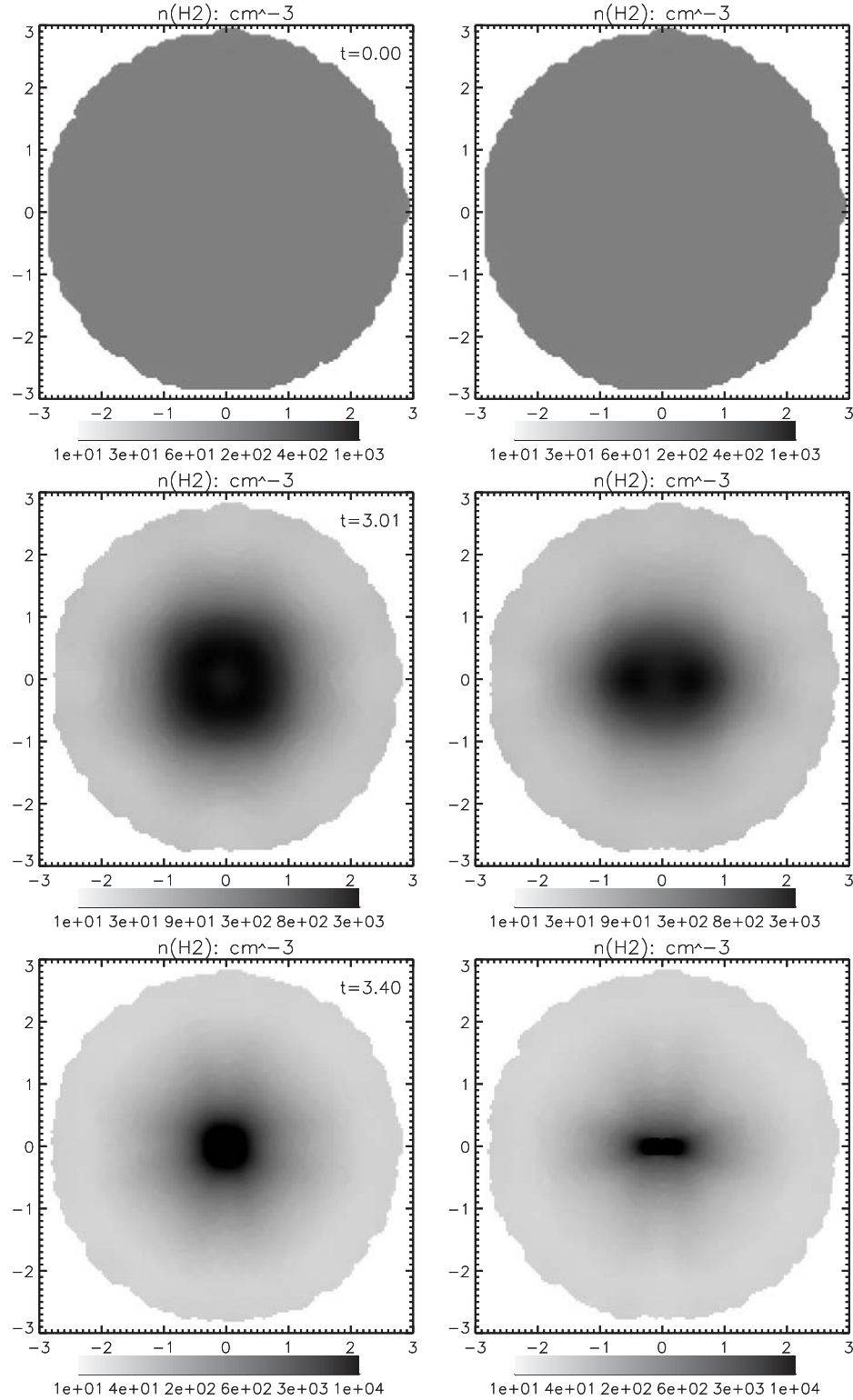


FIG. 6.—This figure shows grayscale images of the density evolution for the  $M = 400 M_{\odot}$ ,  $\delta = 0.5$ , anisotropically heated, spherical cloud. The left panels show values of  $n$  in the  $z = 0$  plane, and the right panels are in the  $y = 0$  plane. Times are shown at the top right corner in units of Myr. Note that the values of  $n$  represented by the grayscale may change from panel to panel.

$z$ -coordinate for particles that lie within a cylindrical distance of  $r = 0.2$  pc from the  $z$ -axis. Comparing the top left panels of Figures 8 and 9, we notice that the maximum temperature of the outside edge of the cloud is  $T \simeq 60$  K in the equatorial regions and  $T \simeq 75$  K at the poles of the cloud. Consequently, the pressure gradient within the cloud

along the  $z$ -direction is greater than along directions in the equatorial plane. As the calculation commences, this causes the cloud to flatten along the  $z$ -direction. As the cloud flattens, the density in the interior increases, and the temperature decreases because of the enhanced attenuation of the UV field. This is illustrated in the top right panels of

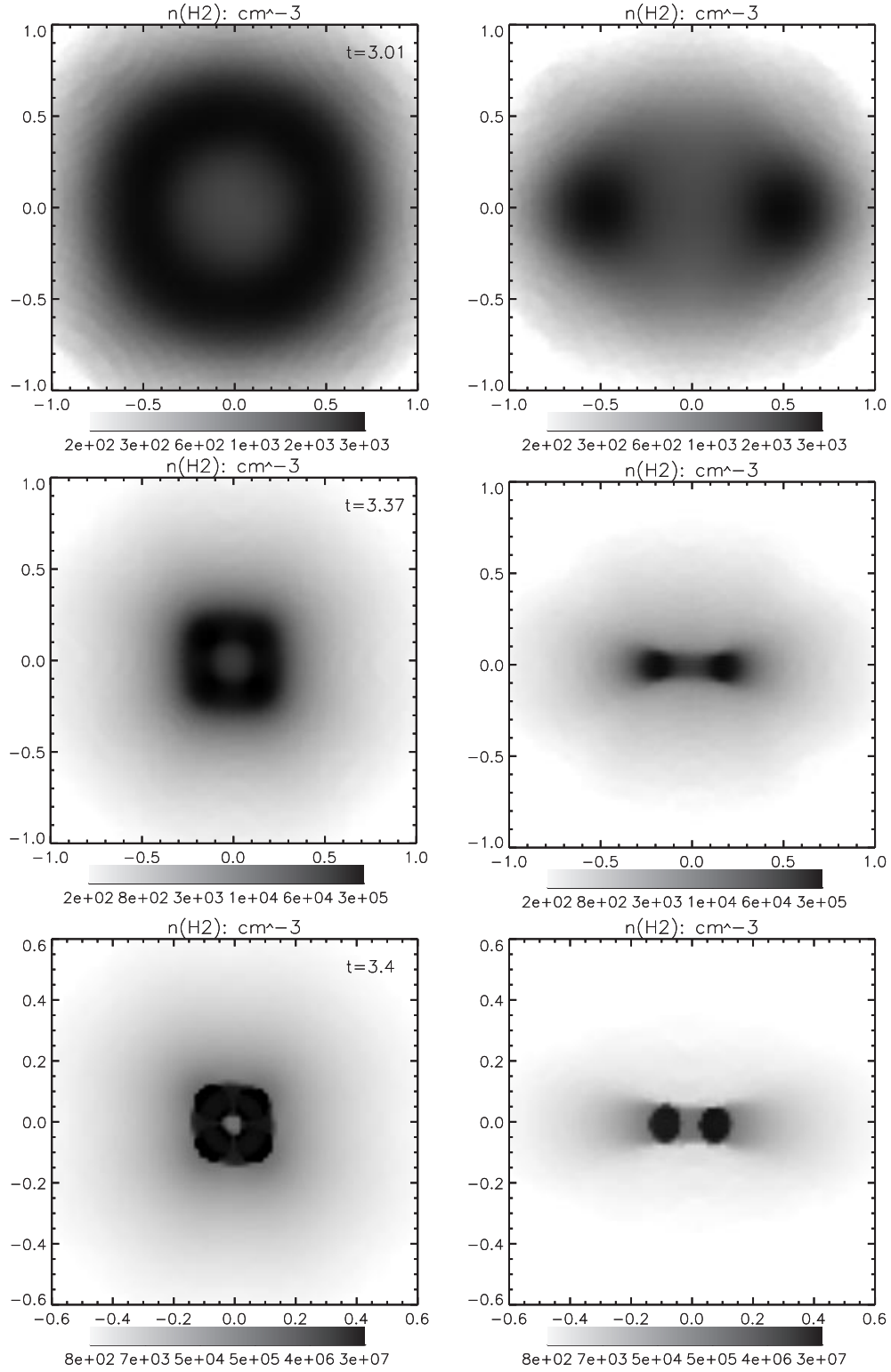


FIG. 7.—This figure shows grayscale images of the evolution of  $n$  for the  $M = 400 M_{\odot}$ ,  $\delta = 0.5$ , anisotropically heated, spherical cloud, where we have zoomed in on the inner regions of the cloud. The left panels show values of  $n$  in the  $z = 0$  plane, and the right panels are in the  $y = 0$  plane. Times are shown at the top right corner in units of Myr. Note that the values of  $n$  represented by the grayscales may change from panel to panel, as may the scaling of the axes.

Figures 8 and 9. Increasing the density and decreasing the temperature allows the local influence of the gravitational forces to increase as the cloud evolves.

At the end of the calculation, the dense core formed at the center of the cloud is highly flattened. It seems unlikely that the differences in the initial pressure forces alone can be

responsible for such a degree of flattening. It is well known that an aspherical distribution of matter, evolving under the influence of gravity and pressure forces, tends to increase its level of asphericity when the ratio of thermal to gravitational energy  $\alpha \simeq 0.25$  (e.g., Nelson & Papaloizou 1993). In order to test whether this is the reason for forming such a

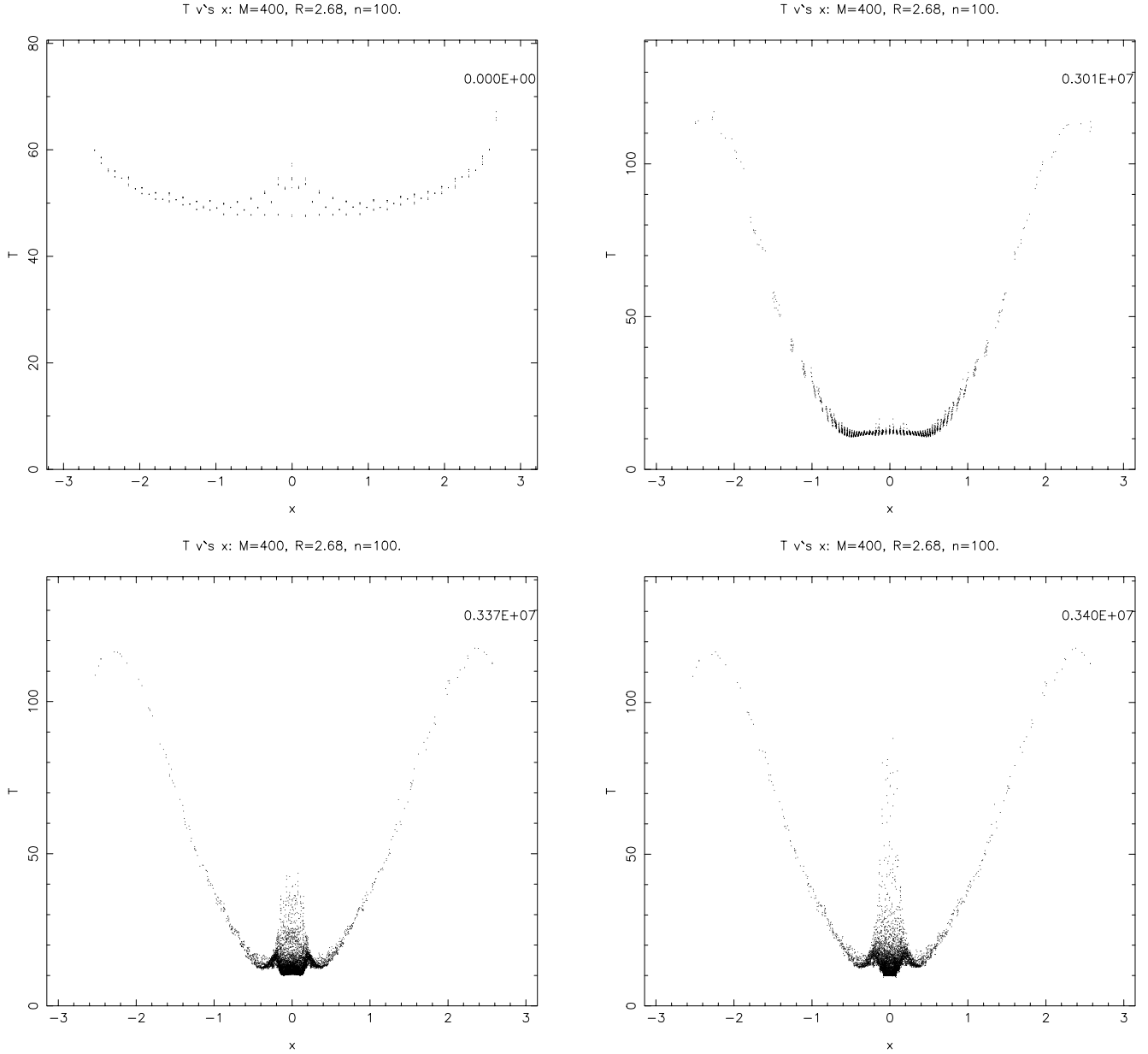


FIG. 8.—This figure shows the evolution of  $T$  as a function of  $x$  for particles located close to the  $x$ -axis of the  $M = 400 M_{\odot}$ ,  $\delta = 0.5$ , anisotropically heated, spherical cloud. Times are shown in the top right corner of each panel in units of years.

dense core, we calculated the values of the thermal and gravitational energy for material interior to a cutoff radius  $R_{\text{cut}} = 0.5$  pc, at different times during the calculation. It was found that  $\alpha$  started off with a high value of  $\alpha \simeq 20$  for material within this subvolume. As time progresses, however,  $\alpha$  drops sharply, so that after  $t = 3.01$  Myr, which corresponds to the top right panel of Figure 6, the top left panel of Figure 7, and the top right panels of Figures 8 and 9,  $\alpha \simeq 0.25$ . Obviously, gravitational forces have become dominant in the central regions by this point, and so are able to amplify the oblateness of the mass distribution, caused initially by the greater pressure present at the poles of the cloud.

In the top right panel of Figure 8, we note that the inner, equatorial region within  $r \approx 0.8$  pc has cooled to a temperature of  $T \simeq 10$  K, whereas the temperature of the gas outside of this radius increases sharply. At the onset of the calculation, the temperature is a maximum at the surface of

the cloud, causing a pressure wave to propagate from the surface toward the center. Since the temperature, and hence the sound speed, in the interior regions of the cloud decreases as a function of time, the pressure wave propagates from a warmer into a cooler medium and steepens into a shock, forming the dense ring observed in the bottom left panel of Figure 7. The temperature of the material in the dense ring is now  $T = 10$  K because the gas is thermally coupled to the dust at these high ( $n > 10^6 \text{ cm}^{-3}$ ) densities. As an aside, we note that the form of the ring structure is not precisely circular in the bottom left panel of Figure 7. This seems to be an artifact of the cloud boundary itself not being spherical but instead being flattened because of the way the particles are distributed on a regular lattice initially. A similar calculation, for which the initial particle setup was randomized, was performed to see if this effect remained. In this case the ringlike structure formed in the dense core showed no sign of the “squareness” present in

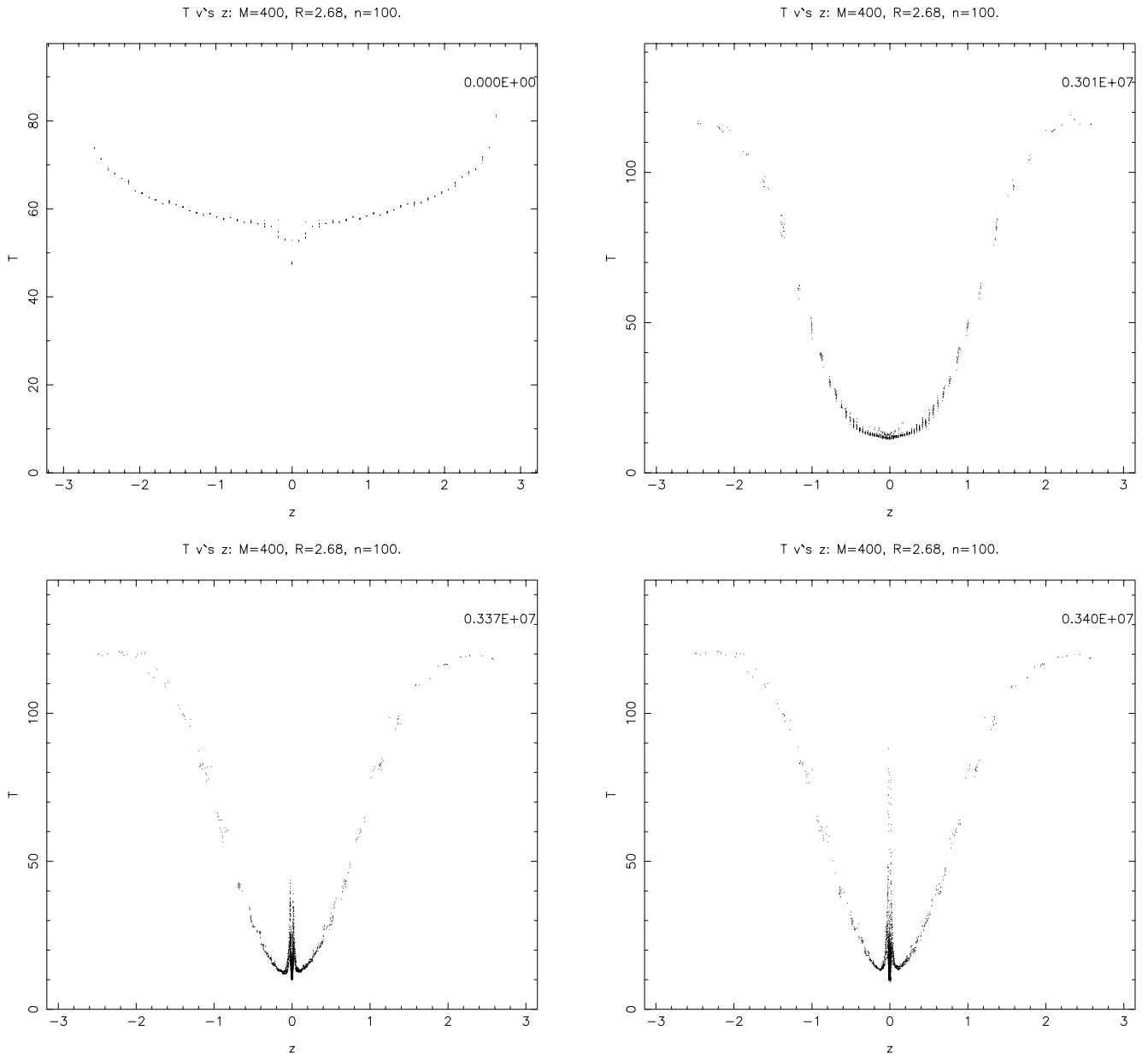


FIG. 9.—This figure shows the evolution of  $T$  as a function of  $z$  for particles located close to the  $z$ -axis of the  $M = 400 M_{\odot}$ ,  $\delta = 0.5$ , anisotropically heated, spherical cloud. Times are shown in the top right corner of each panel in units of years.

the original calculation. The ring structure is gravitationally dominated because of the high densities and low temperatures. Consequently, we expect that it will be unstable to fragmentation into a number of discrete objects (Norman & Wilson 1978). We were unable to continue the calculation to test this hypothesis, however, because the time step size has become too small at this point for efficient computation.

Inspecting the bottom panels of Figures 8 and 9, we notice that there are some particles with higher temperatures in the central regions of the cloud, which in some cases are above  $T = 50$  K. By following the trajectories and thermal history of a subset of these warmer particles, we have ascertained that they originate from regions high above and far below the equatorial plane and are initially located close to the  $z$ -axis. As the cloud collapses, these particles fall toward the equatorial plane because of the flattening of the cloud and are shock heated when they impact with the flattened core, having been accelerated by

the strong gravitational field as they enter the central regions of the cloud. These particles are not contained within the dense, ring structure but instead are located within the lower density regions surrounding the torus. Typically, the density of these particles is  $n \approx 10^4 \text{ cm}^{-3}$ , which is below the density required for the gas-dust cooling to become the dominant thermal process. Consequently, the gas temperature rises as a result of the viscous dissipation and compressional heating, until the molecular line cooling rate is sufficiently high to start overcoming the heating rate. Close inspection of the heating rates indicates that the viscous heating is dominant over the compressional heating for these warmer particles, being typically at least a factor of 2 higher.

As a related aside, we remark that the stochastic shock heating of individual particles to high ( $T > 50$  K) temperatures probably does not mirror the shock heating in a real fluid, where we might expect the shock heating to be

more uniform, but may instead represent a discreteness effect within the simulations. In order to overcome this effect, Monaghan & Lattanzio (1991) introduced a heat diffusion equation into their simulations that effectively allows particles to share the heat generated by shocks, thus avoiding the excessive heating of individual particles. We have not included such a term but note that only a relatively small number of particles are heated to the more extreme temperatures of  $T > 50$  K, and so we do not expect that they play a major role in determining the dynamical evolution of the cloud. Furthermore, while we remain skeptical about the heating of individual fluid elements to temperatures over 50 K, we do believe that, in a qualitative

sense, the shock heating of material falling onto the flattened core represents a real phenomenon.

In a broad sense, the chemical evolution of the cloud is similar to that described previously for the “standard” spherical cloud with an isotropic radiation field. The time evolution of the chemical profile is shown by the grayscale images presented in Figure 10. This figure shows the time evolution of the fractional abundance of CO in both the  $z = 0$  plane (panels in the left-hand column), and in  $y = 0$  plane (panels in the right-hand column). Initially, the cloud contains no CO, but after it has evolved toward a more centrally condensed structure with  $n \approx 10^3$  cm $^{-3}$  in the center, the UV radiation becomes sufficiently attenuated

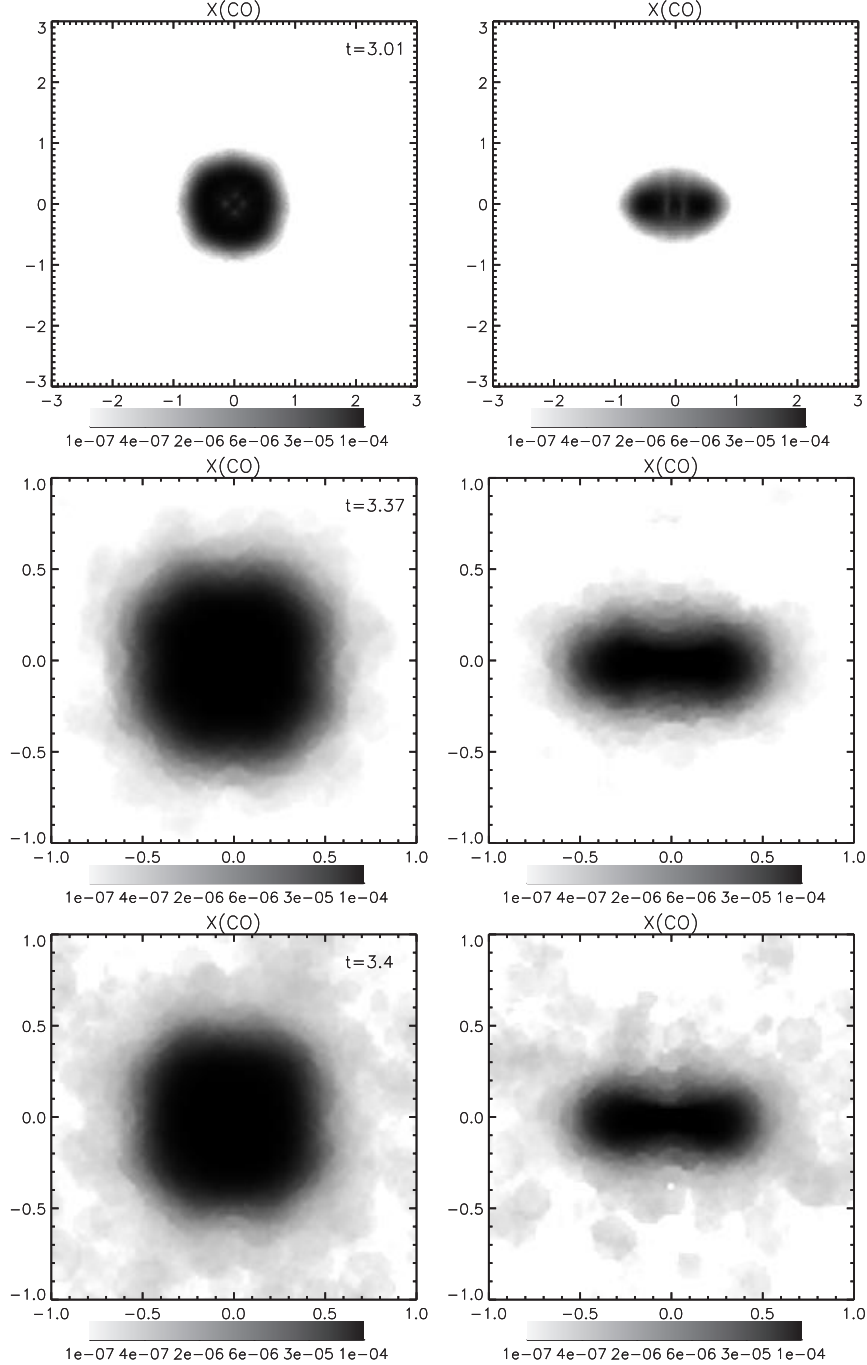


FIG. 10.—This figure shows grayscale images of the evolution of  $X(\text{CO})$  for the  $M = 400 M_{\odot}$ ,  $\delta = 0.5$ , anisotropically heated, spherical cloud. The left panels show values of  $X(\text{CO})$  in the  $z = 0$  plane, and the right panels are in the  $y = 0$  plane. Times are shown at the top right corner in units of Myr. Note that the values of  $X(\text{CO})$  represented by the grayscale may change from panel to panel, as may the scaling of the axes.

that CO is able to survive. The top panels illustrate this early chemical conversion, showing that CO forms only in the inner  $\approx 1$  pc of the cloud. Comparison of these two panels also shows that the region in which the CO is forming has the same flattened morphology as the density field, as one would expect. Another interesting point to note is the fact that there is a slight decrease (by a factor of  $\approx 4\text{--}5$ ) in the fractional abundance of CO in the very central regions of the cloud at this point in time. This arises because of the toroidal structure of the density field at  $t = 3.10$  Myr, which allows radiation to penetrate to the cloud center along its poles, but not along directions in the equatorial plane. Following the chemical evolution further in time, from the middle and bottom panels, one can observe that this decrease in  $X(\text{CO})$  in the center no longer occurs, because the density has increased sufficiently by the continued collapse of the central regions of the cloud to prevent the further penetration of the UV radiation along its poles. (Note that the scaling of the axes has changed in moving from the top right panel to the middle left panel.) The end result of the chemical evolution, then, is the formation of a flattened CO core of radius  $\sim 0.5$  pc and thickness  $\sim 0.2$  pc, surrounded by a halo in which the carbon is in the form of  $\text{C}^+$  and where the minimum UV extinction in any coordinate direction falls below  $\tau_{\text{uv}} \approx 6$ . We note that the chemical transition between the core and halo occurs very sharply, mirroring the sharp increase in density when passing from the cloud envelope into its core.

In a general sense, the outcome of this calculation is similar to the "standard" spherical cloud calculation described in § 5.1, in that a core-halo structure is formed, consisting of a cold, dense, CO core enveloped in a warm, tenuous,  $\text{C}^+$  halo. It is obvious, however, that under certain circumstances, anisotropy in the radiation field can have fairly dramatic effects on the details of the collapse. We have performed calculations on clouds with different parameters than the cloud described in this section. Comparative descriptions of these calculations are given below, in an attempt to draw conclusions about how the details of the collapse are affected by changes in these parameters.

### 5.2.1. Effect of Changing Cloud Masses and Radii

Calculations were performed for clouds with different masses and radii, which were chosen so as to keep the initial number density of the cloud constant at  $n = 100 \text{ cm}^{-3}$ . The different clouds are described in the first paragraph of § 5.2. In each case, the radiation field anisotropy parameter was  $a = 0.5$ .

During each of the runs, the clouds collapsed to form cold, dense, CO cores embedded in warm, tenuous,  $\text{C}^+$  envelopes. The qualitative differences, however, arose in the structure of the dense core formed and, in particular, in the degree of flattening. As a diagnostic of the degree of flattening, we define a parameter,  $e$ , by the relation

$$e = \frac{I_z}{I_{xy}}, \quad (29)$$

where for a fluid continuum

$$I_z = \int_V \rho z^2 dV,$$

$$I_{xy} = \int_V \rho(x^2 + y^2) dV.$$

For a system of discrete particles, these relations become  $I_z = \sum m_i z_i^2$  and  $I_{xy} = \sum m_i (x_i^2 + y_i^2)$ , where  $m_i$  is the particle mass. A spherically symmetric matter distribution should yield a value of  $e = 0.5$ , with objects flattened along their  $z$ -axes yielding values of  $e < 0.5$ . By comparing the different values of  $e$  obtained for different clouds, we can compare the relative degree of flattening present.

Values of  $e$  for each of the three cases are provided in Table 1. These values of  $e$  were calculated by computing the values of  $I_z$  and  $I_{xy}$  for material within a spherical volume whose boundary lay just outside of the dense core. In the case of the  $M = 400 M_\odot$  cloud, this spherical region had a cutoff radius of 0.3 pc. The cutoff radii for the other clouds were chosen such that the ratio of the cutoff radius and the cloud radius were equal to that of the  $400 M_\odot$  case.

The values of  $e$  given in Table 1 correspond to those points in time when the maximum number density in each of the calculations was approximately equal and had just exceeded  $n \approx 10^9 \text{ cm}^{-3}$ . We do not present the values for equal time elapsed, because the clouds evolve at different rates, even though their initial free-fall times are equal (since  $\rho$  is equal at  $t = 0$ ). From the values of  $e$  presented in Table 1, it is apparent that the more massive and larger clouds experience more extreme flattening than lower mass clouds. This correlation in the degree of flattening, as a function of cloud mass and radius, does not seem to be a result of changes in the pressure gradients between the clouds' center and surface as one alters the mass and radius. Instead, it is the gravitational forces within the cloud that are responsible for generating the different degrees of core oblateness, since the relative strength of the gravitational force in more massive clouds is greater.

We note that the  $M = 200 M_\odot$  cloud also displayed the formation of a dense ring in its flattened core, similar to that described in § 5.2 for the  $M = 400 M_\odot$  case. This ring, however, formed closer in toward the center of the cloud, which is to be expected because the strong density increase and strong cooling occurs later on when the pressure wave component traveling in the equatorial plane has propagated further in toward the center.

### 5.2.2. Effect of Changing Anisotropy

We performed a calculation for an  $M = 400 M_\odot$ ,  $R = 2.68$  pc cloud with an anisotropy parameter of  $\delta = 0.2$ , for comparison with the  $\delta = 0.5$  case. The value of  $e$ , calculated using equation (29), obtained for this calculation is

TABLE 1  
CLOUD OBLATENESS

Mass ( $M_\odot$ )	$\delta$	$I_z/I_{xy}$
100.....	0.5	0.300
200.....	0.5	0.073
400.....	0.5	0.063
400.....	0.2	0.226

NOTE.—The first column gives the cloud mass, the second column gives the value of the UV anisotropy, and the third column gives the value of  $e = I_z/I_{xy}$  defined in the text.

given in Table 1. As may be seen from this value, a reduction in the size of the assumed anisotropy parameter leads to a marked decrease in the degree of flattening obtained. This change is to be expected, since the difference between the pressure gradient in the  $z$ -direction compared with that in the equatorial plane is now reduced. Although the degree of flattening is smaller, a significant deviation from spherical symmetry is still obtained with a 20% anisotropy in the UV radiation field. It does not seem unreasonable to expect that some clouds may be subject to UV anisotropies of this order, particularly if they are located above or below the galactic plane. Obviously clouds near massive star-forming regions will experience much greater anisotropies in their incident UV flux, but we do not consider such environments here.

### 5.3. Prolate Clouds

A number of calculations were performed for prolate clouds of different mass and size, subject to heating by an isotropic radiation field. In each case the initial axial ratio was taken to be  $a/b = 2$ , and the number density  $n = 100 \text{ cm}^{-3}$ . Calculations were performed for clouds with masses  $M = 100, 150$ , and  $200 M_{\odot}$ , with their semimajor axes being of length  $a = 2.68, 3.07$ , and  $3.38 \text{ pc}$ , respectively. Only a single calculation was performed for each of the 100 and  $150 M_{\odot}$  clouds. In these cases, the dust temperature was kept at  $10 \text{ K}$ , and the UV radiation flux took the standard interstellar value (i.e.,  $G_0 = 1$ ).

In the case of the  $200 M_{\odot}$  cloud, a number of calculations were performed, with different parameters being changed. A “standard” calculation was performed, with the dust temperature being held at  $T_d = 10 \text{ K}$  and with  $G_0 = 1$ . A calculation was performed with  $T_d = 20 \text{ K}$ , to see if changing the dust temperature altered the qualitative nature of the results. A calculation was performed with  $G_0 = 2$ , and  $T_d = 10 \text{ K}$ , to see how an increase in the radiation field affected the outcome of the calculations. And finally, a calculation was performed with the constant boundary condition being replaced with a free boundary condition, to see how the results depend on the choice of boundary condition. In the discussion that follows below, we will concentrate on the  $M = 200 M_{\odot}$ , semimajor axis  $a = 3.38 \text{ pc}$ ,  $T_d = 10 \text{ K}$ ,  $G_0 = 1$  case, with a constant volume boundary condition. We will provide a brief discussion of the other cases, however, in order to illustrate the general trends observed when the physical parameters are altered.

The results of the  $M = 200 M_{\odot}$ ,  $a = 3.38 \text{ pc}$  “standard” calculation are presented in Figures 11–14. Grayscale images of the number density sampled in the vicinity of the  $z = 0$  plane are presented in Figure 11, where the long axis is taken to be the  $x$ -axis. It should be noted that the scale of the  $x$  and  $y$  axes change from panel to panel, as do the values of  $n$  represented by the grayscale.

Moving from the top left panel to the top right panel of Figure 11, it is apparent that the initially uniform cloud starts to collapse, with the collapse being directed preferentially toward the symmetry ( $x$ ) axis of the cloud. We note that the density field has a maximum followed by a minimum when moving from the surface to the center of the cloud, arising from the propagation of a pressure wave from the cloud surface toward its center. This indicates that the pressure wave is dynamically significant during this initial collapse stage. Following the continued evolution of the

cloud through the remaining panels of Figure 11, it is apparent that a dense, spindle-like core is formed by the continued collapse of the cloud toward its symmetry axis. By the end of the calculation, after a period of  $t = 3.7 \text{ Myr}$ , the dense spindle has fragmented into a number (approximately eight) of high-density subcondensations. At this point in time, the densest fragments have reached number densities of  $10^8\text{--}10^9 \text{ cm}^{-3}$  and are continuing to grow. The calculation was stopped at this point because of the ever-diminishing time step size. We note, however, that the mass contained within these fragments ranges between  $2.5$  and  $7.5 M_{\odot}$ , and they are separated by  $\approx 0.1 \text{ pc}$ .

The thermal evolution of the gas is plotted in Figures 12 and 13 and is broadly similar to that described in the previous calculations for the spherical clouds. Figure 12 displays plots of the particles’ temperature versus their  $x$ -coordinate value at different times during the calculation. Only those particles that lie within a cylindrical distance of  $r = 0.2 \text{ pc}$  of the  $x$ -axis are included in these plots, so that they represent the evolution of the temperature in regions close to the long axis of the cloud. Figure 13 is similar to Figure 12, except that it is a plot of the temperature versus the  $z$ -coordinate, and so represents the thermal evolution of material close to the minor axes of the cloud (assuming near symmetry about the  $x$ -axis).

We note that at the beginning of the calculation, the ratio of the thermal to gravitational energy was  $\alpha = 1.34$ , so that from arguments based on the initial energy content of the cloud, we would not expect it to be gravitationally unstable. A prolate cloud that is marginally stable is expected, from analytical considerations, to contract preferentially along its long axis (Nelson & Papaloizou 1993), becoming less elongated in the process. Numerical calculations have confirmed this (Bonnell, Bate, & Price 1996). It is apparent from Figure 11 that the cloud we are currently considering collapses to form a more elongated spindle and that the ellipticity of the cloud increases rather than decreases. The reason for this appears to be that the pressure gradient between the cloud surface and its center starts to compress the inner parts of the cloud into a more elongated form. Initially, the temperature at the cloud surface is  $T \approx 60 \text{ K}$  and at its center is  $T \approx 40 \text{ K}$ . The subsequent pressure gradient is greater along the short axes of the cloud than along the long axis, because of the differing axis lengths, so that the cloud is subject to a pressure force that accentuates its initial ellipticity. This is illustrated by Figure 15, in which the eccentricity of the cloud ( $e = I_x/I_{yz}$  defined in eq. [29]) is plotted against  $\alpha$  as the cloud evolves. It is apparent that the eccentricity of the cloud increases before it becomes gravitationally unstable, indicating that pressure forces are acting to increase the eccentricity early on in the calculation. As the density starts to increase inside the cloud, the temperature decreases, for reasons already discussed. This may be observed in the top right panels of Figures 12 and 13, where the temperature of material located away from the cloud surface has dropped from  $T \approx 40 \text{ K}$  to  $T \approx 20\text{--}30 \text{ K}$ . Continued evolution of the cloud leads to temperatures reaching  $T \approx 10 \text{ K}$  in the central regions where  $n \approx 10^4 \text{ cm}^{-3}$ . After  $2.8 \text{ Myr}$ , when the minimum temperature is  $T \approx 10 \text{ K}$  and the number density is  $n \approx 10^4 \text{ cm}^{-3}$ , we find that the gravitational forces have become dominant over the pressure forces in the inner  $1.5 \text{ pc}$ , so that the elongated morphology of the density distribution in the inner regions of the cloud, caused by the pressure forces, can now be

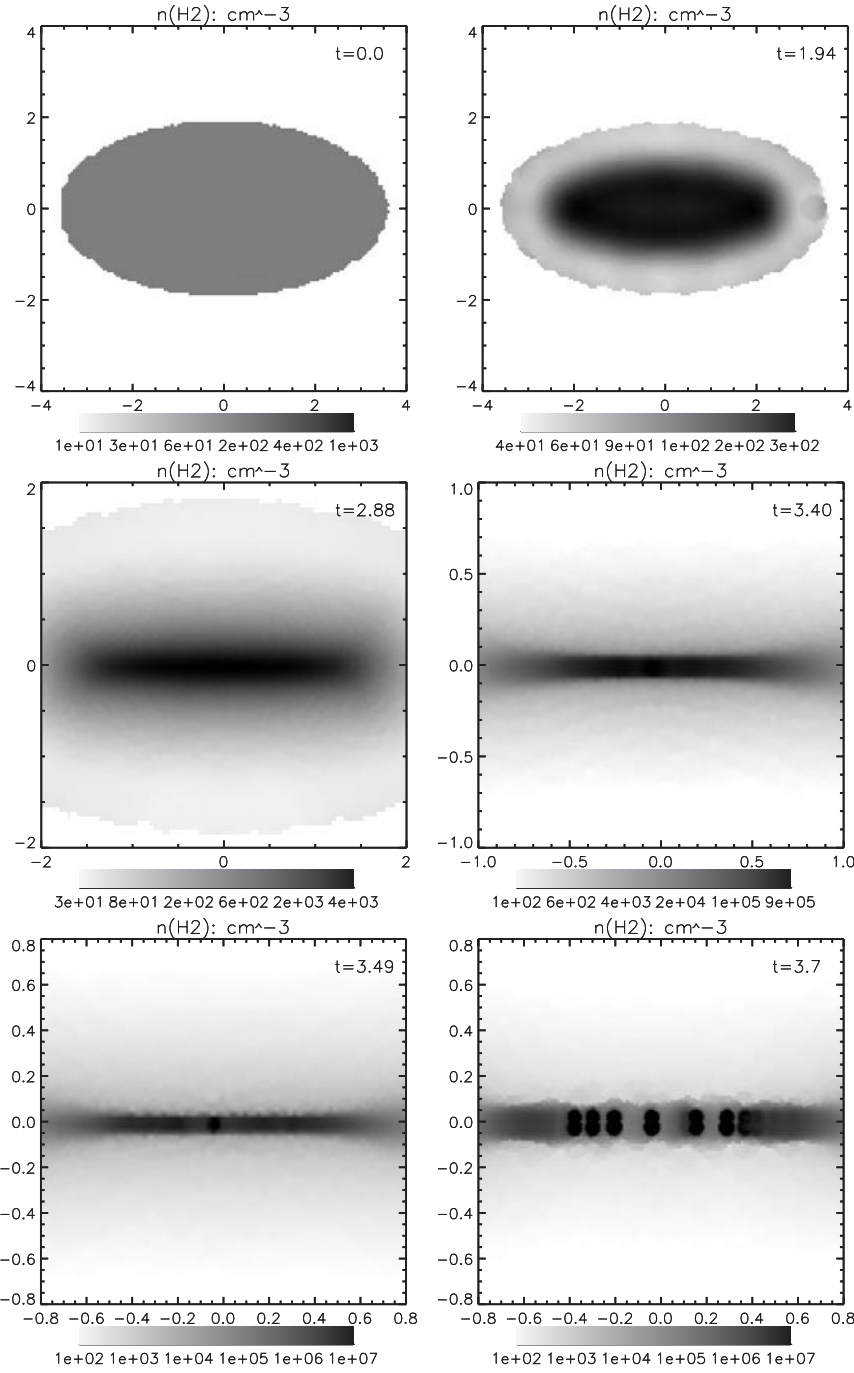


FIG. 11.—This figure shows grayscale images of the evolution of  $n$  for the  $M = 200 M_{\odot}$ , prolate cloud. All panels show values of  $n$  in the  $z = 0$  plane, where the  $x$ -axis is taken to be the long axis. Times are shown at the top right corner in units of Myr. Note that the values of  $n$  represented by the grayscale may change from panel to panel, as may the scaling of the axes.

strongly amplified. Consequently, a cold, self-gravitating spindle is formed by a similar process to that described in Nelson & Papaloizou (1993) and Nelson (1997) when studying the collapse of isothermal, prolate cores. Once the gravitational forces become dominant, the density in the spindle rises rapidly, so that gas-dust cooling becomes the dominant thermal process, the gas remains at  $T = 10$  K, and fragmentation is able to occur.

As in the spherical cloud collapse described in § 5.1, a combination of compressional and viscous heating leads to temperatures rising in the slightly lower density ( $n \approx 10^4$  cm $^{-3}$ ) regions around the spindle during the rapid collapse

stage. This may be seen in bottom right panels of Figures 12 and 13, where the temperature of some particles in the periphery of the spindle rise to between 20 and 30 K.

The chemical evolution is similar to that described in the “standard” spherical case in § 5.1, and as a consequence we provide only a brief description. Grayscale images of the chemical evolution are presented in Figure 14. During the early stages of the collapse, when the density remains below  $n \lesssim 10^3$  cm $^{-3}$ , the carbon remains in the form of C $^{+}$  because the dissociating UV radiation is still able to penetrate through the cloud. As the density rises above  $n \approx 800$  cm $^{-3}$ , the C $^{+}$  starts to react, forming CO molecules. The

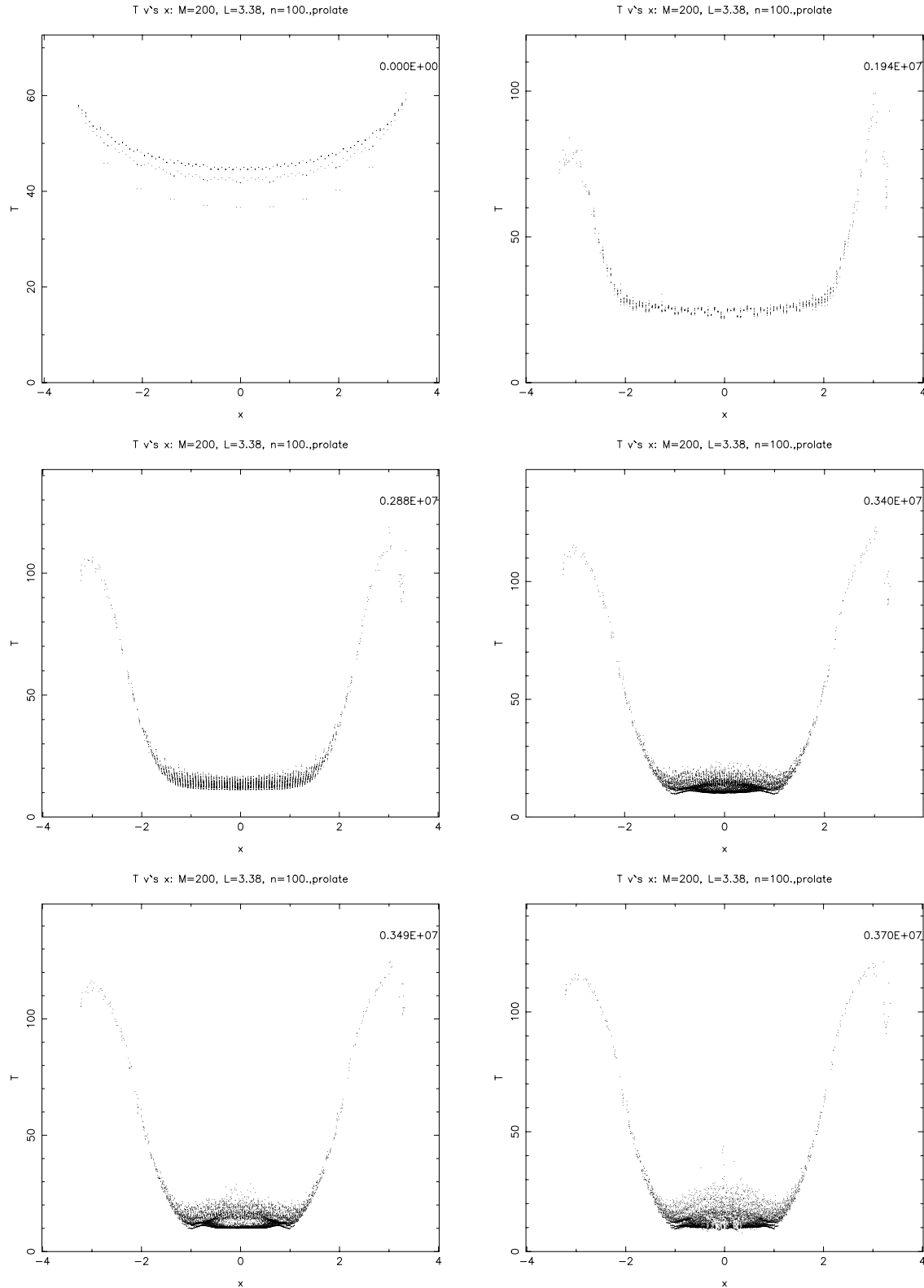


FIG. 12.—This figure shows the evolution of  $T$  as a function of  $x$  for particles located close to the  $x$ -axis of the  $M = 200 M_{\odot}$  prolate cloud. Times are shown in the top right corner of each panel in units of years.

continued rise of the central density leads to the ongoing formation of CO, and by the time the density reaches between  $n = 10^4$  and  $10^5 \text{ cm}^{-3}$ , most of the C<sup>+</sup> in these regions has been converted to CO. Outside of the dense spindle, where the density of material is lower and is more transparent to the incoming UV radiation, the carbon

remains in the form of C<sup>+</sup>, so that we have a dense elongated core in which the carbon is in CO molecules, embedded in an envelope in which the carbon is predominantly in the form of C<sup>+</sup>.

As in the previous examples, this calculation leads to a core-halo structure in terms of the density, thermal, and

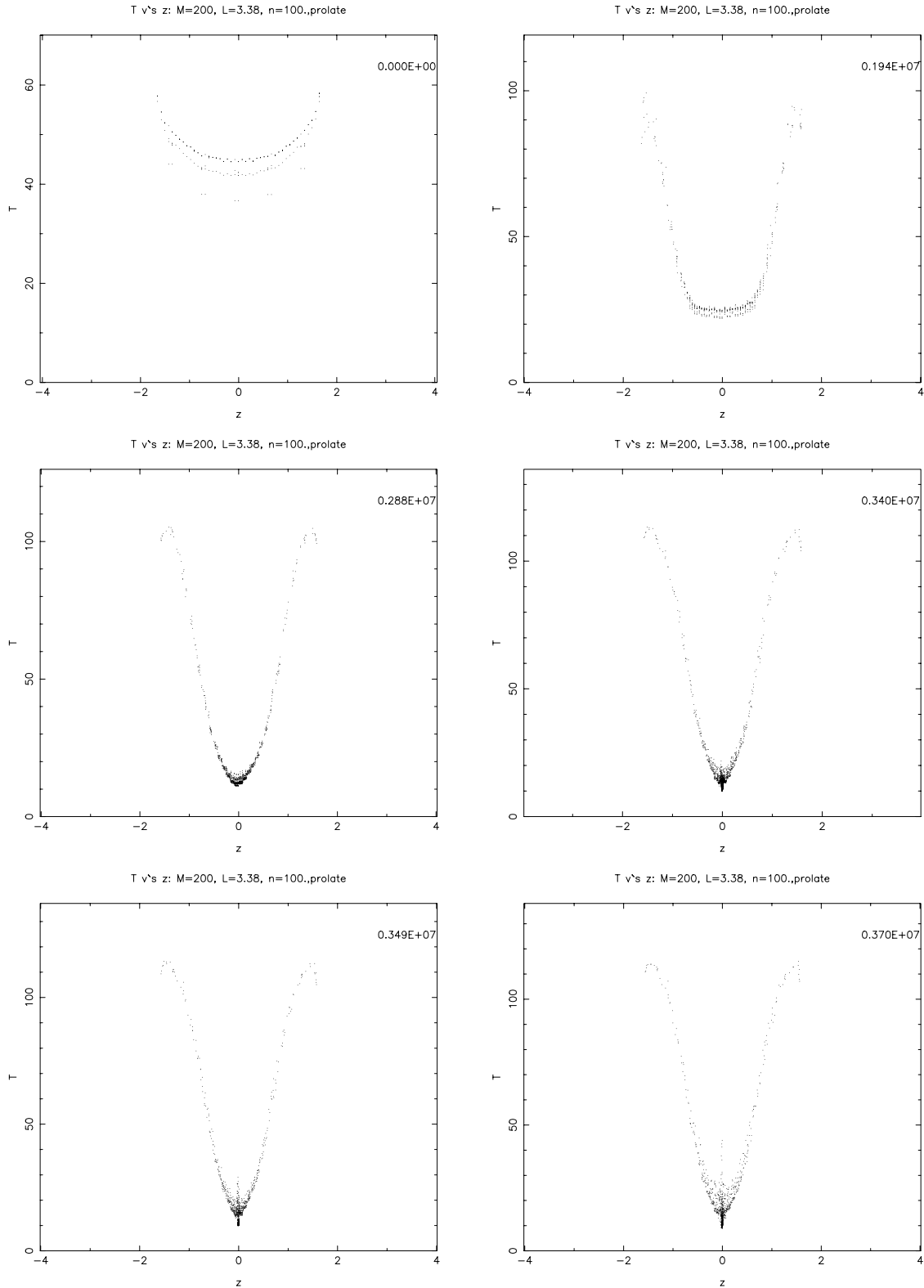


FIG. 13.—This figure shows the evolution of  $T$  as a function of  $z$  for particles located close to the  $z$ -axis of the  $M = 200 M_{\odot}$  prolate cloud. Times are shown in the top right corner of each panel in units of years.

chemical profiles. The difference in this case, however, is that the core formed is a dense, cold spindle, in which the carbon is in the form of CO molecules. The spindle is found to be unstable to fragmentation into a number of subcondensations, so that in this respect the results are similar to the findings of previous numerical and analytical studies

of elongated clouds (Bonnell et al. 1991; Nelson & Papaloizou 1993; Nelson 1997; Boss 1993; Burkert & Bodenheimer 1993). The important difference in this case, however, is that the clouds do not start off being highly unstable to gravitational collapse, but instead must evolve both dynamically and thermally toward such a state. The mass contained

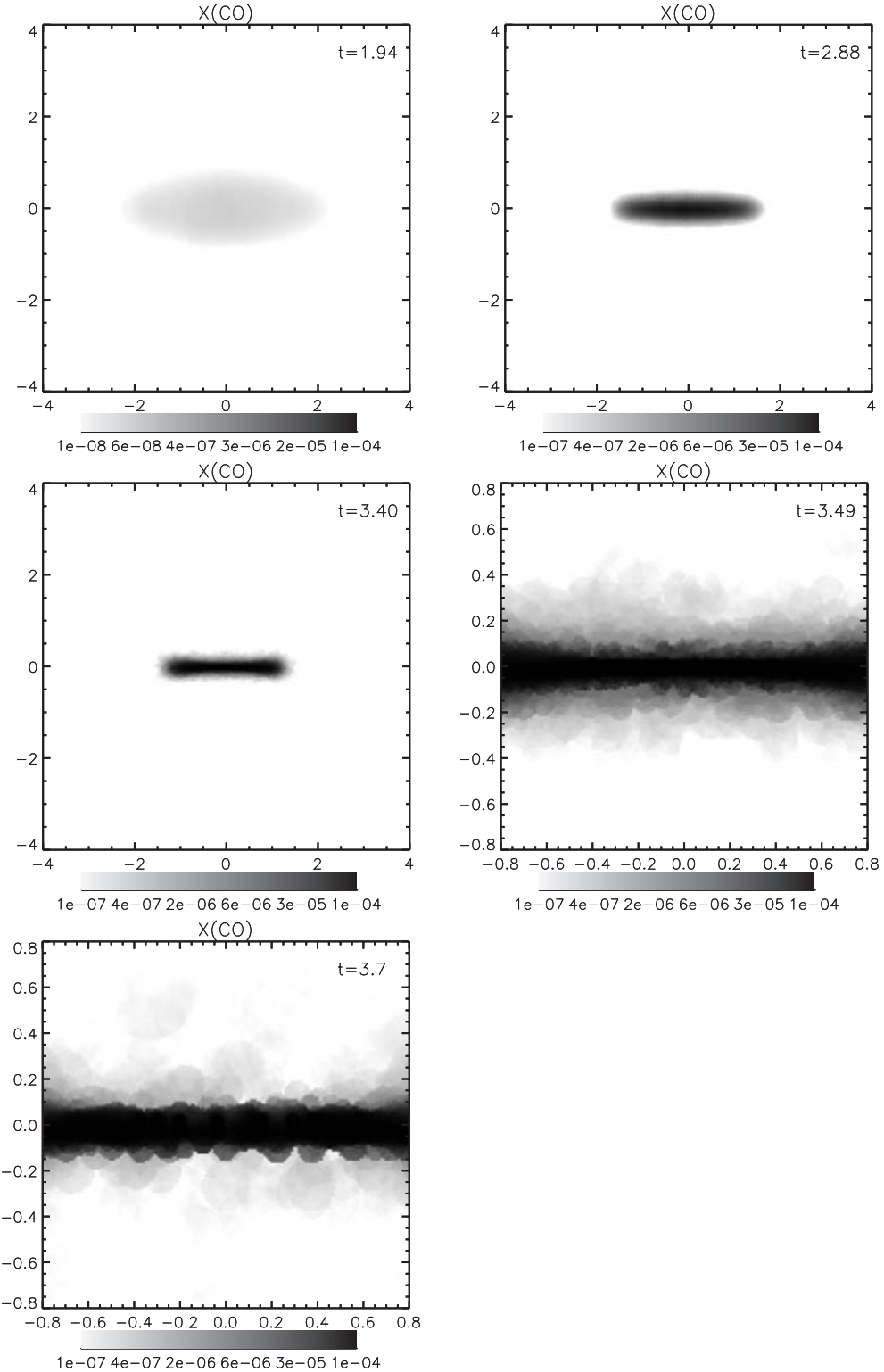


FIG. 14.—This figure shows grayscale images of the evolution of  $X(\text{CO})$  for the  $M = 200 M_{\odot}$  prolate cloud. All panels show values of  $X(\text{CO})$  in the  $z = 0$  plane, where the x-axis is taken to be the long axis. Times are shown at the top right corner in units of Myr. Note that the values of  $X(\text{CO})$  represented by the grayscale may change from panel to panel, as may the scaling of the axes.

within these fragments is between  $2.5$  and  $7.5 M_{\odot}$ , which is typical of dense, cold cloud cores in low-mass clouds.

#### 5.3.1. Effect of Changing Cloud Mass and Size

Additional calculations were performed with clouds of mass  $M = 100$  and  $150 M_{\odot}$  and with semimajor axes of length  $a = 2.68$  and  $3.07$  pc. The dust temperature and UV

flux were taken to be the same as in the “standard”  $M = 200 M_{\odot}$  calculation. The early evolution of these calculations was similar to the “standard” prolate case, in that the existence of a temperature gradient caused the propagation of a pressure wave into the cloud interior, leading to the formation of an elongated core. The end results of the calculations, however, were found to be qualitatively differ-

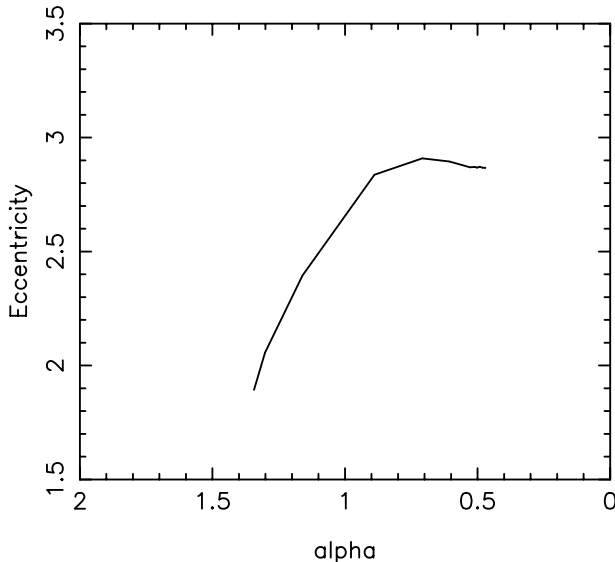


FIG. 15.—This figure shows the evolution of the cloud eccentricity as a function of  $\alpha$  for the  $M = 200 M_\odot$  prolate cloud.

ent. This difference lies in the degree of elongation of the central core formed toward the end of the calculations and its subsequent evolution. The  $M = 100 M_\odot$  cloud produced a core that was considerably less elongated than the “standard” prolate case, and the  $M = 150 M_\odot$  cloud produced a core that, while being slightly less elongated than that of the  $M = 200 M_\odot$  case, was considerably more elongated than that of the  $100 M_\odot$  cloud. This result again stems from the fact that the gravitational forces are more dominant in larger mass clouds than in lower mass clouds.

No fragmentation of the core in the  $100 M_\odot$  cloud was found to occur. Instead, the densest region of the core was quasi-spherical in shape and was surrounded by a less dense, but elongated, envelope whose density was  $n \sim 10^4 \text{ cm}^{-3}$ . Spherical cores are known to be stable against fragmentation (e.g., Larson 1985). The elongated core in the  $150 M_\odot$  cloud was found to be unstable to fragmentation, producing three well-defined subcondensations. The masses of these fragments were between 5 and  $7.5 M_\odot$  at the end of the calculation.

### 5.3.2. Effect of Dust Temperature

A calculation was performed for an identical cloud, except that the dust temperature was taken to be  $T_d = 20 \text{ K}$ . As expected, the early evolution of this cloud followed that of the “standard”  $M = 200 M_\odot$  prolate spheroid, since the gas-dust coupling does not become important until densities have reached  $n \gtrsim 10^5 \text{ cm}^{-3}$ . Thus, the cloud collapses to form a self-gravitating spindle structure. At densities of  $n \approx 10^4 \text{ cm}^{-3}$ , the gas temperature is  $T \approx 10 \text{ K}$ , since the molecular line cooling and the cosmic-ray heating approximately balance one another in this region of the density-temperature plane (see Fig. 1). As the spindle becomes increasingly more dense, however, the gas-dust coupling becomes increasingly important and the dust begins to heat the gas. At densities  $n > 10^6 \text{ cm}^{-3}$ , the temperature within the spindle rises to  $T = 20 \text{ K}$ . With this additional pressure support present within the spindle, it contains fewer Jeans masses and so is less unstable to gravitational breakup than the  $T = 10 \text{ K}$  spindle formed in the previous calculation.

Consequently, it is found that the spindle forms only about four fragments in this case, whereas the previous calculation produced about eight. The mass contained within the fragments, however, is found to about the same, ranging from approximately  $4$  to  $7 M_\odot$ .

### 5.3.3. Effect of Increasing Radiation Field

We performed a calculation for an  $M = 200 M_\odot$ ,  $L = 3.38 \text{ pc}$  cloud, with the dust temperature  $T_d = 10 \text{ K}$  and with the UV radiation flux twice the standard interstellar value (i.e.,  $G_0 = 2$ ). In this case, the initial temperature profile within the cloud was changed by the increased heating rate, with the surface temperature being  $T \approx 82 \text{ K}$  and the central temperature being  $T \approx 48 \text{ K}$ . During the early stages of the evolution, the gas remained warmer than in the “standard”  $M = 200 M_\odot$ ,  $G_0 = 1$  prolate cloud calculation, but the existence of the pressure gradient between the outer and inner parts of the cloud still resulted in a compression wave propagating into the cloud interior. With the additional heating, and hence the increased temperatures, the gravitational forces became dominant over the pressure forces at a slightly later time than in the similar calculation in which  $G_0 = 1$ . The result of this additional heating is that the elongation of the spindle structure was reduced, with that part of the cloud reaching  $n \geq 10^6 \text{ cm}^{-3}$  extending over only  $\approx 0.8 \text{ pc}$ , whereas in the  $G_0 = 1$  case, the region of the cloud that reached densities of  $n \geq 10^6 \text{ cm}^{-3}$  extended over  $\approx 1.2 \text{ pc}$ . The reduction in the length of the spindle structure results in a reduced ability to fragment, since its linear extent contains a smaller number of Jeans lengths, so that the number of fragments formed in this case was about four as compared with about eight in the  $G_0 = 1$  case.

### 5.3.4. Effect of Changing Boundary Conditions

We repeated the “standard”  $M = 200 M_\odot$  prolate cloud calculation with a free boundary condition rather than a constant volume condition, in order to test the effect that the boundary may have on the simulations. One effect that may be expected to arise from using a constant volume boundary condition is that the action of the inward-propagating pressure wave might be increased by the presence of a barrier against which the gas can push, so that the tendency to collapse and form a dense spindle may be reduced by its removal. Our calculation, however, indicates that the use of a constant volume boundary condition has little effect on the outcome of the calculations. The qualitative nature of the collapse remained the same, with the formation of a dense, cold spindle at the center of the cloud. The spindle was found to fragment, with about seven subcondensations being formed, similar to the eight condensations formed in the constant volume boundary case. Thus, although the quantitative details of the results are changed slightly by using a different boundary condition, their qualitative nature is not. We note that three varieties of boundary condition are often used in hydrodynamic calculations: constant volume, constant pressure, or free, where a constant pressure condition in a sense represents an intermediate between the first and the last of these. Presumably similar results would be obtained if we were to use a constant pressure boundary condition.

Although the behavior of the central regions of the cloud are not affected to a large degree by the boundary condition employed, the outer regions certainly are. In this calculation, it is observed that the outer layers of the cloud

expand away from the cloud center in the absence of a confining boundary. As they do so, the material becomes more diffuse, leading to an increase in the temperature since the C<sup>+</sup> and O I cooling becomes less efficient at lower densities. Under these circumstances, our cooling becomes dominated by the artificial cooling described in equation (10), so that we are unable to provide a realistic discussion of the evolution of the outer cloud layers.

#### 5.4. Oblate Clouds

A number of calculations were performed for clouds with oblate geometries. In each case, the axial ratio of the clouds was  $a/b = 2$  and the initial number density was  $n = 100 \text{ cm}^{-3}$ . The masses of the clouds were  $M = 100, 200$ , and  $400 M_{\odot}$ , and their semimajor axes were  $a = 2.13, 2.68$ , and  $3.38 \text{ pc}$ , respectively. The short axis is assumed to be the  $z$ -axis. The dust temperature was taken to be fixed at  $T_d = 10 \text{ K}$ , and the interstellar radiation field was given its standard value of  $G_0 = 1$ . In the discussion that follows below, we will concentrate on the  $M = 400 M_{\odot}$ ,  $a = 3.38 \text{ pc}$  case, since it gave rise to the most interesting results of the three calculations. The other remaining calculations are discussed briefly, however, in order to illustrate the trends in behavior obtained when the mass and radii of oblate clouds are changed.

The evolution of the number density is illustrated by the grayscale images presented in Figures 16a and 16b. It should be noted that the scaling of the axes changes when moving between some of the panels, as do the values of  $n$  represented by the grayscale. Panels in the left-hand column contain grayscale images of the number density sampled in the vicinity of the  $z = 0$  plane, and those in the right-hand column are images sampled in the vicinity of the  $y = 0$  plane. Following the evolution of the cloud, it is apparent that it collapses preferentially along its  $z$ -axis, forming a flattened disklike core. Closer inspection of this core (Fig. 16b) shows that the flattened core has developed significant substructure, indicative of gravitational fragmentation. This substructure first becomes apparent when the peak number density rises above  $n \gtrsim 10^5 \text{ cm}^{-3}$ . The bottom left panel of Figure 16b best illustrates the degree of fragmentation, where approximately eight fragments may be observed. We note that the initial ratio of thermal to gravitational energy in this cloud was  $\alpha = 0.84$ , so that although the cloud started off as a bound configuration, one would not expect it to collapse to form such a flattened structure if the gas were unable to cool.

Figures 17 and 18 show the time evolution of the temperature profile. Figure 17 is a plot of temperature versus the  $x$ -coordinate value and contains only those particles that lie within a cylindrical distance from the  $x$ -axis of  $r = 0.2 \text{ pc}$ . Because of the initial near symmetry of the calculation, this figure then represents the thermal evolution in the equatorial plane of the cloud. Figure 18 is a similar figure, except that it is a plot of temperature versus the  $z$ -coordinate value and represents the thermal evolution of material close to the polar axis of the cloud. As the density in the interior of the cloud increases, due to the surface pressure gradient and the cloud relaxing in its own gravitational potential well, the temperature there starts to decrease, as is illustrated by comparing the top panels of Figures 17 and 18. After about 3 Myr of evolution, the peak number density has risen to  $n \sim 10^4 \text{ cm}^{-3}$ , and the minimum temperature has dropped to  $T \simeq 13 \text{ K}$ . Contin-

ued increase of the density leads to decreasing minimum temperatures to  $T \simeq 10 \text{ K}$  and an increase in the local dynamical influence of the gravitational forces. The initial generation of the flattened structure in the density field of the cloud interior arises for reasons similar to those described in § 5.3 when discussing the evolution of the prolate clouds. Once again, the gravitational forces become dominant in the inner regions of the cloud, and are responsible for the formation of the dense, flattened structure observed in Figure 16 and its eventual fragmentation. As in the previous calculations, the region outside the dense core consists of warm, low-density gas.

The chemical evolution is once again similar to that which arose in the previous calculations and is shown in Figure 19 as a grayscale image of  $X(\text{CO})$ , the fractional abundance of CO. The panels in the left-hand column are images of  $X(\text{CO})$  sampled in the vicinity of the  $z = 0$  plane. Those in the right-hand column are images sampled in the vicinity of the  $y = 0$  plane. It should be noted that the scale of the axes changes when moving from the middle right panel to the bottom left panel. Initially, the carbon is in the form of C<sup>+</sup> and remains so until the cloud has evolved toward a more centrally condensed structure. The top panels show the initial formation of CO after the cloud has evolved for  $\simeq 3 \text{ Myr}$ , where the peak value of  $X(\text{CO}) \simeq 5 \times 10^{-5}$ . It is apparent that the CO is confined to the dense, inner regions of the cloud and has a morphology that mirrors that of the flattened density field. Continued evolution of the cloud leads to increased formation of CO, until we are eventually left with a cold, dense, CO core, surrounded by a warm, tenuous, C<sup>+</sup> halo.

Calculations have been performed previously for *isothermal* oblate clouds. Bastien (1983) calculated the collapse of finite cylinders, whose lengths were shorter than their diameters, using a two-dimensional hydrodynamics code. These calculations led to the formation of a dense, flattened structure, in which a dense ring was found to form, perhaps as a result of a boundary effect propagating inward as the calculations proceeded. Boss (1996) performed calculations in three dimensions for oblate spheroids. These calculations led to the formation of a dense, flattened structure toward the cloud center, which underwent subsequent fragmentation, similar to that observed in the calculation described above.

##### 5.4.1. Effect of Changing Mass and Radius

The other two calculations involving oblate clouds showed quite different qualitative behavior from the  $M = 400 M_{\odot}$  case. The  $100 M_{\odot}$  cloud was found to collapse to form a *prolate* core at its center. In this case, the collapse of the cloud occurred more strongly in  $x$ - $y$  plane than along the  $z$ -direction, so that the dense core that was formed by the end of the calculation was elongated in the  $z$ -direction. This mode of collapse is expected in an oblate object that is unstable to collapse but whose gravitational forces are not strong enough to dominate the pressure forces along the minor axis (i.e., the Jeans length is longer than its linear extent along the  $z$ -direction). Thus, as the density in the central regions increased and the temperature decreased, the gravitational forces did not become sufficiently dominant that they could induce strong collapse along the  $z$ -axis. The initial oblateness of the cloud, however, allows strong collapse along the  $x$ - and  $y$ -directions, causing material in the more equatorial regions

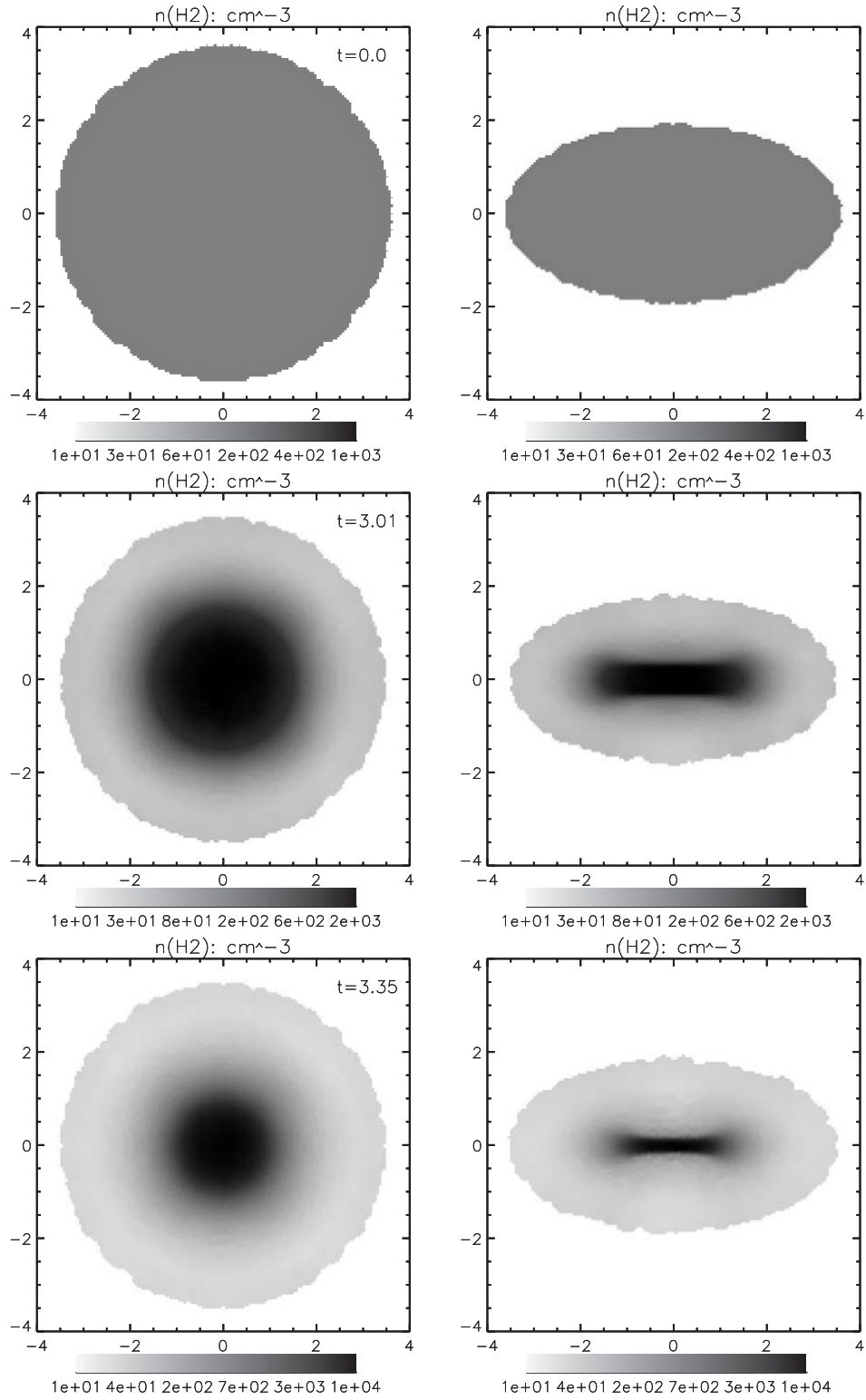


FIG. 16a

FIG. 16.—This figure shows grayscale images of the evolution of  $n$  for the  $M = 400 M_{\odot}$  oblate cloud. The left panels show values of  $n$  in the  $z = 0$  plane, where the  $z$ -axis is taken to be the short axis. The right panels are in the  $y = 0$  plane. Times are shown at the top right corner in units of Myr. Note that the values of  $n$  represented by the grayscale may change from panel to panel, as may the scaling of the axes.

to be accelerated rapidly toward the cloud center. The  $M = 200 M_{\odot}$  cloud collapsed to form a flattened core structure similar to that observed in Figure 16. The larger mass of this cloud, and of the  $400 M_{\odot}$  cloud, allowed the gravitational forces in the central regions of the cloud to dominate the pressure forces along the  $z$ -direction once the density in

the central regions had increased and the temperature had decreased. The  $200 M_{\odot}$  cloud showed no signs of fragmentation, but instead had a single density maximum located at the cloud center. In this case, the gravitational forces were not sufficiently dominant to cause a strong enough collapse in the  $z$ -direction such that a disk could be formed that was

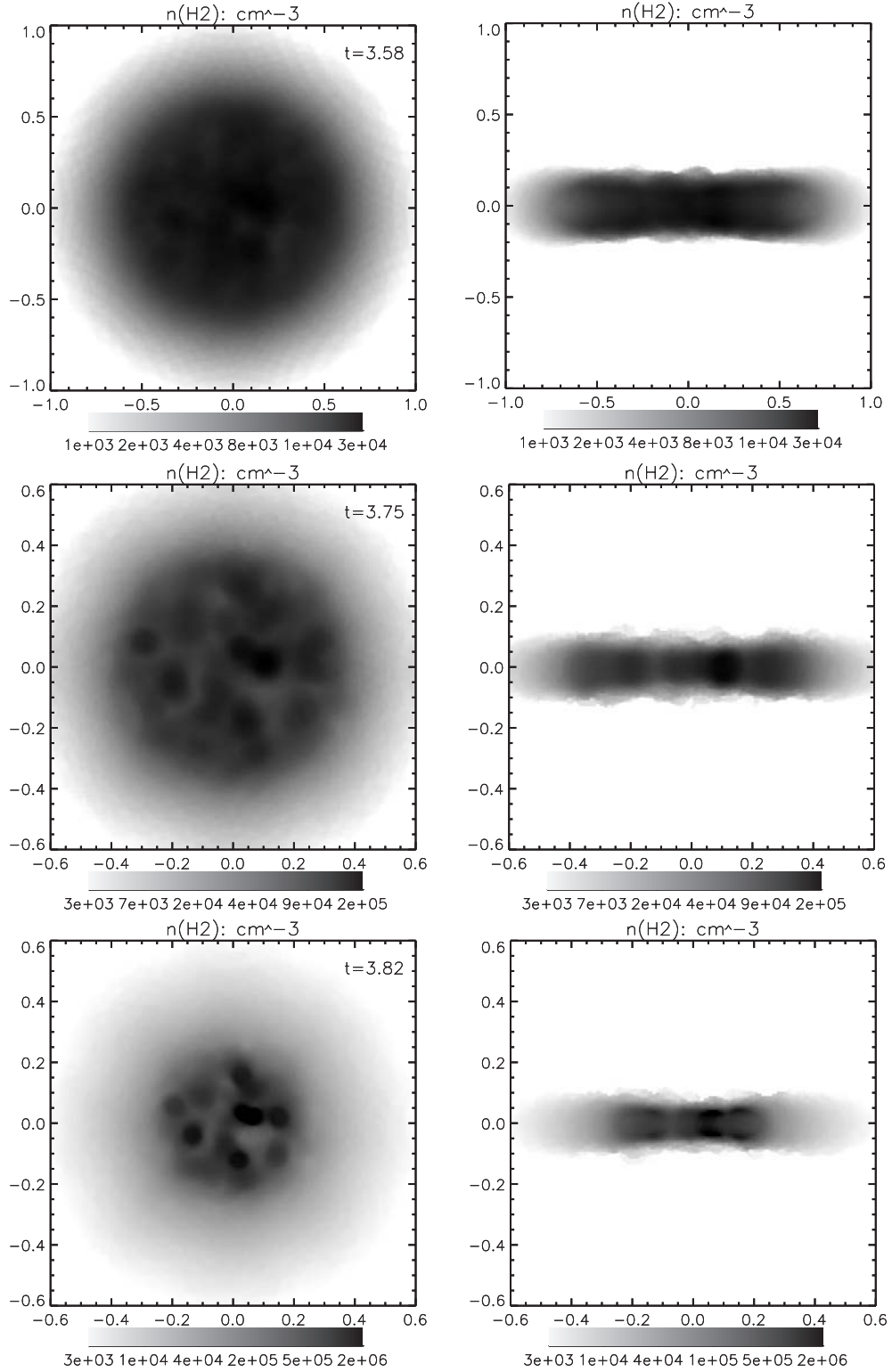


FIG. 16b

unstable to fragmentation. In the  $400 M_\odot$  case, the gravitational forces were obviously dominant enough that the core formed was able to flatten to a degree necessary to allow fragmentation.

## 6. DISCUSSION AND CONCLUSIONS

We have presented the results of calculations that follow the dynamical, thermal, and chemical evolution of isolated,

low-mass molecular clouds. These calculations, where the cloud support is provided by thermal pressure alone, represent the first step in the development of a class of models for the evolution of molecular clouds from an initially diffuse state to one in which there exist higher density structures. These models are therefore applicable to the isolated globules that have been the subject of a number of recent observational surveys (Clemens & Barvainis 1988; Clemens

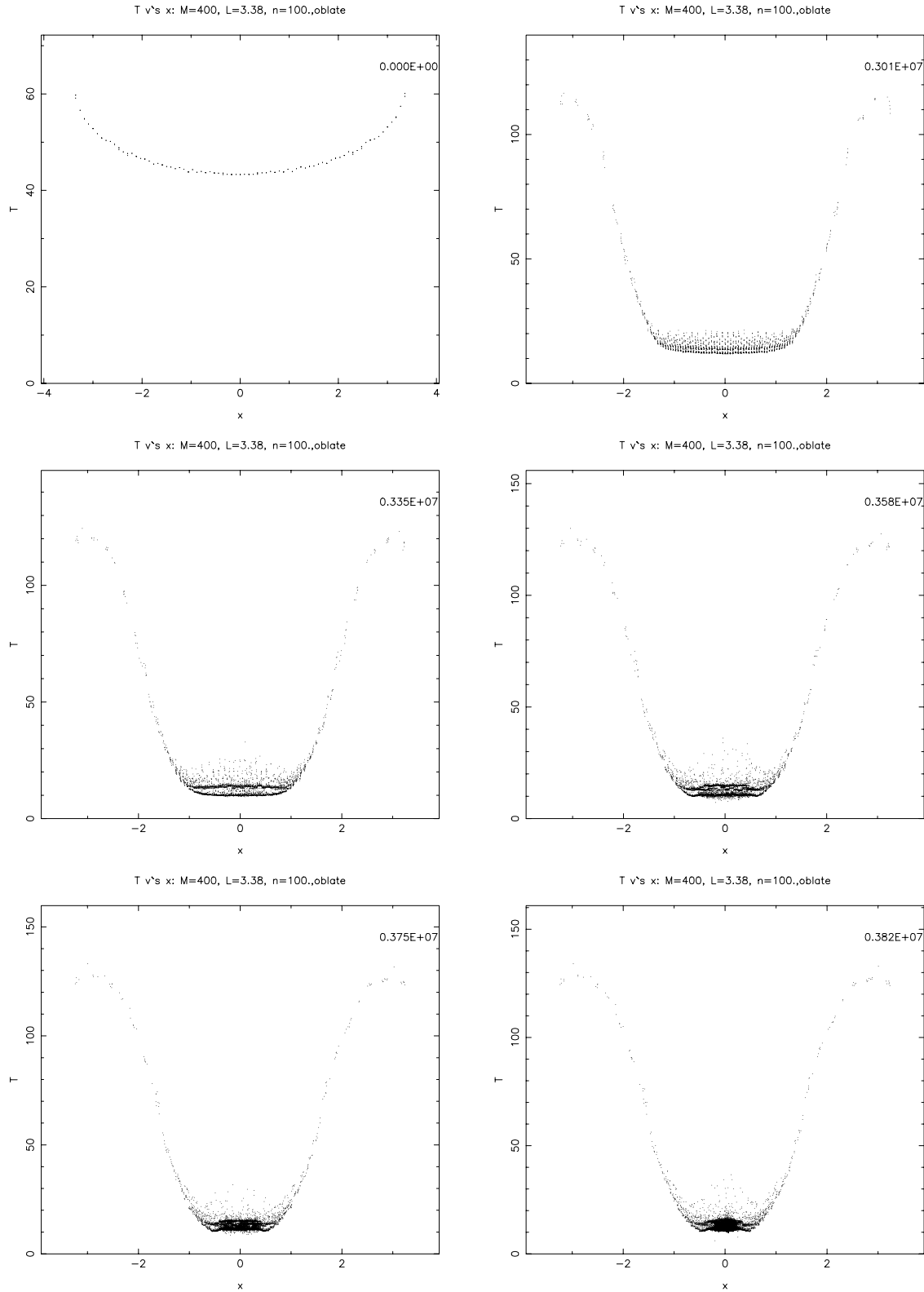


FIG. 17.—This figure shows the evolution of  $T$  as a function of  $x$  for particles located close to the  $x$ -axis of the  $M = 400 M_{\odot}$  oblate cloud. Times are shown in the top right corner of each panel in units of years.

et al. 1991; Bourke et al. 1995a, 1995b).

The main results of the calculations are as follows:

1. A cloud whose thermal support is initially such that it is not expected to undergo gravitational collapse may do so by virtue of it being able to cool as it evolves toward a more centrally condensed structure.

2. A pressure gradient is set up between the cloud surface and center because of the attenuation of the external UV field as it penetrates the cloud. Although this gradient in itself is unable to initiate the collapse of a cloud, it nonetheless can have significant impact on the morphological evolution of a cloud. In particular, when a spherical cloud is

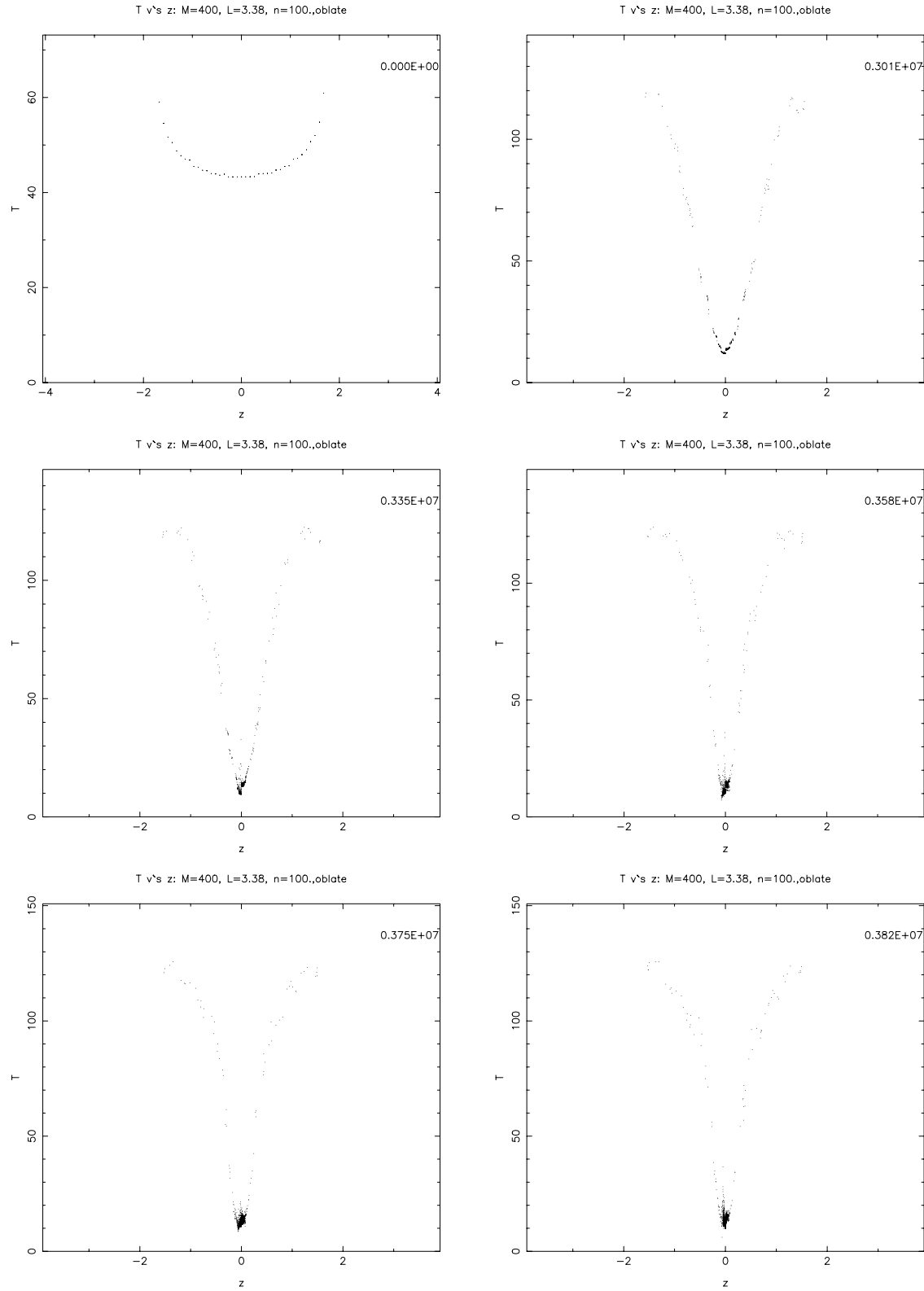


FIG. 18.—This figure shows the evolution of  $T$  as a function of  $z$  for particles located close to the  $z$ -axis of the  $M = 400 M_{\odot}$  oblate cloud. Times are shown in the top right corner of each panel in units of years.

subject to an anisotropic UV field, the cloud forms a cold, dense, flattened core, where the minor axis of this core points along the direction of greatest UV radiation intensity. The continued propagation of a pressure wave, from the cloud surface, in directions orthogonal to the minor axis

of the dense core leads to the formation of a dense toroidal structure. This occurs because the wave steepens into a shock as it enters the cooler central regions of the cloud. Observations of the Thumbprint Nebula (Lehtinen et al. 1995), which is located below the Galactic plane, indicate

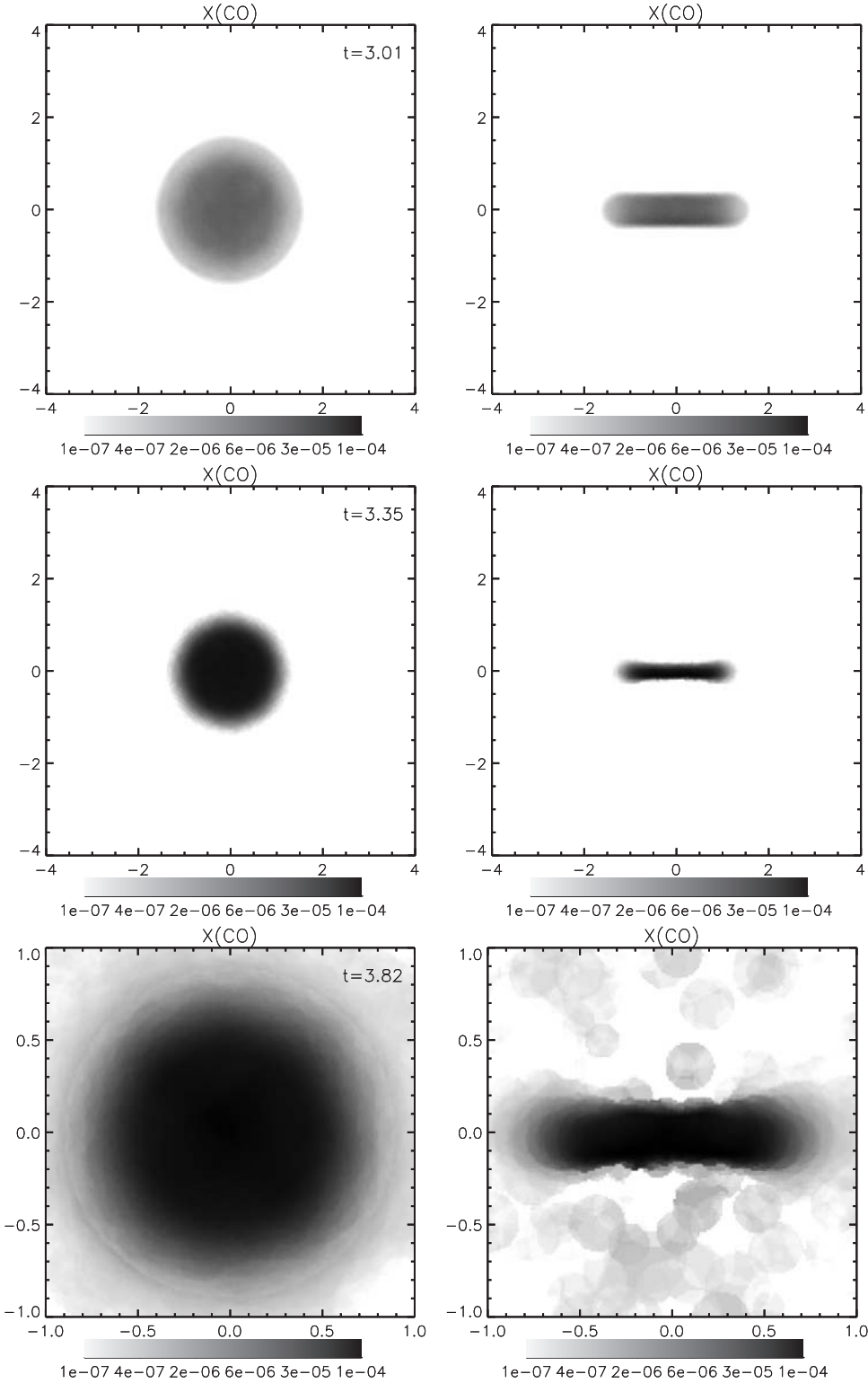


FIG. 19.—This figure shows grayscale images of the evolution of  $X(\text{CO})$  for the  $M = 400 M_{\odot}$  oblate cloud. The left panels show values of  $X(\text{CO})$  in the  $z = 0$  plane, where the  $z$ -axis is taken to be the short axis. The right panels are in the  $y = 0$  plane. Times are shown at the top right corner in units of Myr. Note that the values of  $X(\text{CO})$  represented by the grayscale may change from panel to panel, as may the scaling of the axes.

that an anisotropic radiation field can have significant effects on the morphology and chemical evolution of an isolated globule.

3. Initially nonspherical clouds, subject to isotropic radiation fields, are found to form nonspherical, dense cores at their center. A prolate cloud forms an elongated spindle,

whereas an oblate cloud forms a flattened disklike structure. These aspherical cores appear to be the result of the pressure gradients between the surface and center compressing the density field morphology in the central regions of the clouds. The increase in density in these regions leads to a reduction in the temperature there and, hence, to an

increase in the local influence of the gravitational forces. Eventually, gravity is able to amplify the asymmetry in the density field, leading to the formation of highly nonspherical structures.

4. The formation of elongated or flattened cores can lead to the fragmentation of the cloud into an number of objects, where this number depends on the mass of the cloud. This arises because the formation of dense, nonspherical structures facilitates the breakup of a cloud, since the fastest growing mode of collapse in these cases is some fraction of the linear extent of the cloud (Larson 1985). Although isolated globules are usually associated with the formation of single or binary stars, recent observations of the isolated cloud CB 34 (Alves & Yun 1995) indicate the formation of a small stellar cluster.

5. The number of fragments formed is typically between four and eight. Larger numbers of fragments are formed in the higher mass rather than the lower mass clouds, and their mass is usually between 3 and  $8 M_{\odot}$ .

6. The chemical evolution of a cloud begins when the dissociating UV radiation starts to be attenuated. In our models, the complete conversion of  $C^+$  to CO occurs in the central regions of the cloud when the number density rises beyond  $n \gtrsim 10^3 \text{ cm}^{-3}$  and when  $\tau_{\text{uv}}$  is about a few. It appears, however, that the chemical change has little effect on the cloud dynamics. This is because the cooling rate of  $C^+$  is not that dissimilar to that of CO, particularly in the region of the density-temperature plane at which the chemical conversion takes place (i.e.,  $n \sim 10^3\text{--}10^4 \text{ cm}^{-3}$ ,  $T \sim 10\text{--}20 \text{ K}$ ).

7. The final outcome of all our calculations is the formation of a cold, dense, CO core, surrounded by a warmer, tenuous,  $C^+$  halo. The dense core is typically  $r \sim 0.2 \text{ pc}$  in size and contains about 1/5 of the total mass. For example,

in the standard spherical case ( $M = 100 M_{\odot}$ ,  $R = 1.69 \text{ pc}$ ) presented in § 5.1, the dense ( $n \geq 10^3 \text{ cm}^{-3}$ ) CO core contains about  $21 M_{\odot}$  in a volume of radius 0.25 pc. This value is similar to the masses and radii derived, using CO observations, for the isolated globules studied by Clemens et al. (1991). Here, the mean mass of molecular material was estimated to be  $M \sim 11 M_{\odot}$  and the mean radius  $r \sim 0.35 \text{ pc}$ . Our calculations, however, indicate that most of the cloud mass is in a nonmolecular envelope and so may not be detectable by observations of molecular line transitions.

To develop a more detailed understanding of how the coupled dynamical-thermal-chemical effects lead to the formation of the complex structure and protostellar cores observed in low- to intermediate-mass molecular clouds, it will be necessary to extend the calculations presented here to include additional processes. In subsequent work, we will examine how the inclusion of nonthermal support provided by random motions, rotation, and magnetic pressure affect the outcome of the calculations. We will also look into how the initial density profile affects the evolution of the clouds, since the relaxation of uniform clouds in their gravitational potential wells appears to affect the outcome of the results. We are currently working on an improved model for the chemical and thermal evolution of the photodissociation region.

Richard Nelson is a National Research Council Research Associate. This research was conducted at the Jet Propulsion Laboratory, California Institute of Technology, under support from the National Aeronautics and Space Administration. We would like to thank Alan Boss and John Papaloizou for useful discussions during the course of this work.

## REFERENCES

- Alves, J. F., & Yun, J. L. 1995, *ApJ*, 438, L107  
 Arcoragi, J.-P., Bonnell, I., Martel, H., Benz, W., & Bastien, P. 1991, *ApJ*, 380, 476  
 Barnes, J., & Hut, P. 1986, *Nature*, 324, 446  
 Bastien, P. 1983, *A&A*, 119, 109  
 Bate, M. B., Bonnell, I., & Price, N. M. 1995, *MNRAS*, 277, 362  
 Beichmann, C., Myers, P. C., Emerson, J. P., Harris, S., Mathieu, R., Benson, P. J., & Jennings, R. E. 1986, *ApJ*, 307, 337  
 Bergin, E. A., Langer, W. D., & Goldsmith, P. F. 1995, *ApJ*, 441, 222  
 Binney, J., & Tremaine, S. 1987, in *Galactic Dynamics*, ed. J. P. Ostriker (Princeton: Princeton Univ. Press), 291  
 Bonnell, I., Bate, M. R., & Price, N. M. 1996, *MNRAS*, 279, 121  
 Bonnell, I., Martell, H., Bastien, P., Arcoragi, J. P., & Benz, W. 1991, *ApJ*, 377, 553  
 Boss, A. P. 1986, *ApJS*, 62, 519  
 ———. 1993, *ApJ*, 410, 157  
 ———. 1996, *ApJ*, 468, 231  
 Bourke, T. L., Hyland, A. R., & Robinson, G. 1995a, *MNRAS*, 276, 1052  
 Bourke, T. L., Hyland, A. R., Robinson, G., James, S. D., & Wright, C. M. 1995b, *MNRAS*, 276, 1067  
 Burkert, A., & Bodenheimer, P. 1993, *MNRAS*, 264, 798  
 Charnley, S. B., Dyson, J. E., Hartquist, T. W., & Williams, D. A. 1988, *MNRAS*, 231, 269  
 Chieze, J. P., & Pineau des Forets, G. 1987, *A&A*, 183, 98  
 Christodoulou, D. M., & Tohline, J. E. 1990, *ApJ*, 363, 197  
 Clemens, D. P., & Barvainis, R. 1988, *ApJS*, 68, 257  
 Clemens, D. P., Yun, J. L., & Heyer, M. H. 1991, *ApJS*, 75, 877  
 de Jong, T. 1997, *A&A*, 35, 137  
 Falgarone, E., & Puget, J.-L. 1985, *A&A*, 142, 157  
 Genzel, R. 1991, in *Space Chemistry*, ed. J. M. Greenberg & V. Pirronello (Dordrecht: Kluwer), 123  
 Gerola, H., & Glassgold, A. E. 1978, *ApJS*, 37, 1  
 Gingold, R. A., & Monaghan, J. J. 1977, *MNRAS*, 181, 375  
 Glassgold, A. E., & Langer, W. D. 1976, *ApJ*, 204, 403  
 Goldsmith, P. F., & Langer, W. D. 1978, *ApJ*, 222, 881 (GL78)  
 Goodman, A. A., Benson, P. J., Fuller, G. A., & Myers, P. C. 1993, *ApJ*, 406, 528  
 Graedel, T. E., Langer, W. D., & Frerking, M. A. 1982, *ApJS*, 48, 321  
 Habing, H. J. 1968, *Bull. Astron. Inst. Neth.*, 19, 421  
 Herbst, E., & Leung, C. M. 1986, *MNRAS*, 222, 689  
 Hernquist, L. 1987, *ApJS*, 64, 715  
 Hernquist, L., & Katz, N. 1989, *ApJS*, 70, 419  
 Langer, W. D. 1976, *ApJ*, 206, 699  
 Larson, R. B. 1985, *MNRAS*, 214, 379  
 Laureijs, R. J., Fukui, Y., Helou, G., Mizuno, A., Imaoka, K., & Clark, F. O. 1995, *ApJS*, 101, 87  
 Lehtinen, K., Mattila, K., Schnur, G. F. O., & Prusti, T. 1995, *A&A*, 295, 487  
 Loren, R. B. 1989, *ApJ*, 338, 902  
 Lucy, L. 1977, *AJ*, 83, 1013  
 Millar, T. J., Herbst, E., & Charnley, S. B. 1991, *ApJ*, 369, 147  
 Monaghan, J. J., & Lattanzio, J. C. 1991, *ApJ*, 375, 177  
 Monaghan, J. J., & Varnas, S. R. 1988, *MNRAS*, 231, 51  
 Myers, P., & Benson, P. 1983, *ApJ*, 266, 309  
 Myers, P., Fuller, G. A., Goodman, A. A., & Benson, P. J. 1991, *ApJ*, 376, 561  
 Myhill, E. A., & Kaula, W. M. 1992, *ApJ*, 386, 578  
 Nelson, R. P. 1994, Ph.D. thesis, Queen Mary and Westfield College, London  
 ———. 1997, *MNRAS*, submitted  
 Nelson, R. P., & Papaloizou, J. C. B. 1993, *MNRAS*, 265, 905  
 ———. 1994, *MNRAS*, 270, 1  
 Norman, M. L., & Wilson, J. R. 1978, *ApJ*, 224, 497  
 Prasad, S. S., Heere, K. R., & Tarafdar, S. P. 1991, *ApJ*, 373, 123  
 Prasad, S. S., & Huntress, W. T., Jr. 1980, *ApJS*, 43, 1  
 Ryden, B. S. 1996, *ApJ*, 471, 822  
 Tarafdar, S., Prasad, S., Huntress, W., Villere, K., & Black, D. 1985, *ApJ*, 289, 220  
 Tohline, J. E., Bodenheimer, P. H., & Christodoulou, D. M. 1987, *ApJ*, 322, 78  
 Xie, T., Allen, M. A., & Langer, W. D. 1995, *ApJ*, 440, 674